Estimation of creep strain and creep failure of a glass reinforced plastic by semi-analytical methods and 3D numerical simulations

F. Lavergne, Karam Sab, Julien Sanahuja, Michel Bornert, Charles Toulemonde

Estimation of creep strain and creep failure of a glass reinforced plastic by semi-analytical methods and 3D numerical simulations.

F. Lavergne[a], K. Sab[a,*], J. Sanahuja[b], M. Bornert[a], C. Toulemonde[b]

[a] *Laboratoire Navier, Université Paris-Est, ENPC, IFSTTAR, CNRS 77455 Marne-la-Vallée Cedex, France*
[b] *Département Mécanique des Matériaux et des Composants, EDF R&D, Site des Renardières, Avenue des Renardières, 77818 Moret-Sur-Loing Cedex, France*

Abstract

Glass reinforced plastics based on Polyvinyl chloride (PVC) is a material of choice for construction applications, such as pipes. The lifetime of pipes may be limited by creep failure and polymers exhibit a viscoelastic response that depends on the time of loading. In this paper, homogenization methods are designed to upscale the viscoelastic properties of a composite material made of chopped glass fibers with random orientations and PVC. The estimates of the Mori-Tanaka scheme and 3D numerical computations for creep strains and creep failure are compared, validating the Mori-Tanaka model as a practical tool to predict the effect of fiber length and volume fraction of fibers on creep strain and creep failure. In particular, it appears that, for a given creep load, the lifetime of the material is increased if the volume fraction of fibers increases or if the length of fibers decreases, as long as the failure mode is fiber breakage.

Keywords:
creep, polymer, aging, homogenization

Introduction

Polyvinyl chloride (PVC) is a material of choice for construction applications, such as pipes for water and gas, house sidings or window frames where long service life is required [1]. The European demand of PVC was 5000 ktons in 2012 [2]. Many polymers may be part of composite materials, such as fiber-reinforced materials. For instance, glass fibers may be incorporated into a polymer matrix

*Corresponding author. Tel: +33 1 64 15 37 49
Email address: karam.sab@enpc.fr (K. Sab)
Postprint of Mechanics of Materials doi:10.1016/j.mechmat.2015.06.005

such as PVC to increase stiffness, creep resistance and dimensional stability [3, 4, 5]. The effect on tensile strength of glass fibers depends on the volume fraction of inclusions, on the fiber length and on fiber orientation. These parameters can be significantly affected by processing operations[6, 7].

In case of water pipes, different permanent loads coexist. Cooling after extrusion could trigger internal tensile stress in the range 1.5 to 4.8MPa on the inner diameter, the water pressure induces a permanent hoop stress and additional stresses can occur as a result of non-uniform soil settlement [8]. The lifetime of such pipes depends on the operating conditions and on the mechanical properties of the constitutive materials.

Glass reinforced plastic pipes may feature a complex structure, including chopped strand mat layers on the inner side and filament wound layers on the outer side [9, 10, 11]. Short-time hydraulic failure occurs on the inner diameter [10]. Ring deflection tests may be performed according to standard ISO 9967 to estimate the time-dependent strain of a pipe and study the long term creep failure [12, 9]. In this case, failure mode was always the same, fiber breakage, and always localized in the same region, on the inner diameter [9]. The strain at failure is almost constant, slightly decreasing with the time elapsed since loading. An internal pressure test is defined by the standard ASTM D2992 to estimate the long term static hydrostatic strength of glass-fiber-reinforced pipes [13]. The time-to-failure is expected to depend on the pressure level, following a power law. Hence, studying the viscoelastic behavior of glass reinforced plastics is required to adjust delayed fracture criterion [14] and estimate the lifetime and durability of such pipes.

Polymers exhibit a viscoelastic response that depends on the time of loading t'. This phenomenon is described as physical aging. It is well known that the viscoelastic properties of polymer glasses are significantly influenced by a physical aging process[15, 16, 17]. This is the reason why the standard ISO 9967 specifies both the temperature (23$\pm$2°C) and the age of the samples at loading (21$\pm$2 days), measured since quenching. Experimental evidences on creep properties of various polymer materials below the glassy temperature have been gathered by Struik [15] and further creep tests have been performed on PVC since [18, 19]. A PVC quenched from 90°C to 20°C at starting time $t_0 = 0$ is considered in the present study.

This article is focused on the aging creep and failure of the chopped mat strand layer of the pipe, modeled as a composite material made of E-glass fibers and PVC. Homogenization methods are designed to upscale the viscoelastic behaviors of such materials. Mean-field homogenization schemes such as the one of Mori-Tanaka [20, 21, 22] or coupling the single fiber problem and the rule of mixture [7] produce estimates of these elastic properties while taking account of fiber aspect ratio and distribution of orientations. Complete modeling of the failure

of fiber-reinforced plastics, including damage of fibers and matrix, have been performed by Sasayama et. al. [23] and Hashimoto et. al. [24]. Some of these micromechanical approaches have recently been able to treat aging linear viscoelastic materials and their accuracy is to be checked by numerical simulations [25, 26, 27].

Mean-field homogenization schemes and 3D numerical simulations of matrix-inclusion materials have been compared in the range of elasticity [28, 29, 30, 31]. The case of elongated or flat inclusions has been explored [28, 29, 30] with the conclusion that Lielen's model [32] was the most accurate one provided that the inclusion is stiffer that the matrix. Such comparisons have also been performed on viscoelastic [33], plastic [34] or viscoplastic [35, 33] matrices to assess the accuracy and performances of different methods. Lahellec and Suquet [33] have used 2D full finite element simulations to validate a semi-analytical scheme which combines the Hashin-Shtrikman estimate for periodic materials and a time-stepping procedure to compute the in-plane time-dependent strain of aligned circular fibers in a viscoelastic matrix. The range of applications of such models depends on the contrast between phases and volume fraction of inclusions.

The objective of the present article is to estimate the aging viscoelastic behavior and creep failure of a E-glass fiber reinforced PVC. Therefore, the Mori-Tanaka scheme is to be compared to full-field computations. The main features of the model presented in this article are :

1. Both the Mori-Tanaka scheme and the 3D numerical procedure rely on a time-shift procedure to account for the aging creep of PVC.
2. The Mori-Tanaka scheme and a 3D numerical procedure are presented and successfully compared.
3. The influence of volume fraction of fibers and length of fibers are investigated.
4. An estimate of creep failure related to the strength of glass fiber, based on the largest principal stress (Rankine criterion), is proposed.

The behavior of each phase is described and the microstructure is presented in the first section. The methods to obtain the overall property are briefly recalled. The outputs of these methods are compared in the second section and the effect of the length of fibers and of the volume fraction of fibers on the time dependent strain and creep failure are estimated.

1. Microstructure : geometry and mechanical properties

1.1. A short-fiber reinforced plastic

The polymer-based composite that is described in the present article will be a mix of hard PVC and short E-glass fibers. Figure 1a shows the microstructure of the considered material[3].

In the considered fiber-reinforced material, elastic inclusions are added to the viscoelastic matrix, their elastic stiffness being the one of E-glass fibers : the Young modulus is $E = 80$GPa and the Poisson's ratio is $\nu = 0.22$ [36, 37, 38]. These inclusions are assumed to be cylindrical chopped fibers, with a diameter of 10μm and a length of 100μm. The distribution of their directions is chosen as isotropic and their volume fraction is 15%. The density of E-glass being about 2.55 and the one of PVC being about 1.35, a weight ratio of 34 phr (part per hundred part of resin) corresponds to a volume fraction of 15%. Above 50 phr (or 20% volume fraction), processing difficulties may appear during the extrusion [3].

The considered chopped strand mat features shorter fibers than the one used in automotive applications [39] (11mm to 75mm) or pipes, comparable to fibers used for flooring materials(0.2mm to 1mm) [40]. The considered microstructure could be similar to the one obtained by the use of chopped strand glass as reinforcement in extruded products, where the integrity of the dry glass fiber strands is broken down by a screw extruder [41, 5, 42, 43].

1.2. Failure mode

Experimental tests have shown that the lifetime of a pipe under permanent loading decreases as the level of the applied loading increases [12, 9]. Moreover, the strain at failure decreases slightly with respect to lifetime. The failure mode of a glass fiber-reinforced PVC highly depends on the coupling agent[3] : the observed failure mode of water pipes was fiber breakage located at points where the largest tensile stress occurred [9]. These experimental evidences will drive the proposed estimates of the lifetime of a pipe using the Mori-Tanaka procedure described in this paper. Indeed, it is assumed that the fibers are perfectly bonded to the matrix until failure occurs.

A fiber is considered as brittle, and a maximum stress criterion is defined to describe its failure [24]. The large variability in strength found in brittle fibers [44] is well modeled by Weibull-Poisson statistics and is due to various random flaws on the fiber surface [45]. Moreover, the strength of glass fibers is a function of time when subject to permanent loads [46] : moisture ingress in glass fiber reinforced polymers increases stress corrosion cracking in the fibers [47, 48, 49, 50, 51] and thus shortening their lifetime in humid or alkali environments [52, 53]. Nevertheless, for the seek of simplicity, these features will be ignored in the present study and the same uniform-in-time maximum stress criterion σ_c will be set for all fibers.

Let $\sigma_R(\sigma)$ be the largest principal stress of the stress tensor σ. Then the scalar Rankine criterion stipulates that the failure occurs if $\sigma_R(\sigma) > \sigma_c$. This criterion coincides with Hashimoto's one [24] in case of uniaxial tensile stress in the fiber.

1.3. Aging linear viscoelasticity

The strain tensor $\varepsilon(t)$ in a viscoelastic material depends on the history of stress tensor $\sigma(t)$. If the constitutive law is linear, the Boltzmann superposition principle states that the material properties are defined by a compliance function (fourth order tensor), $\mathbf{J}(t,t')$, such that :

$$\varepsilon(t) = \int_0^t \mathbf{J}(t,t')\frac{d\sigma}{dt}(t')dt'$$

If the elapsed time since loading is the only relevant parameter, the material is non-aging :

$$\mathbf{J}(t,t') = \mathbf{\Phi}(t-t')$$

Non-aging compliance may be approximated by a series of Kelvin chain, which arises from a rheological model made of springs and dashpots (Fig. 2). The advantage of a series of Kelvin chain is that internal variables may be defined, which eases numerical computations. Its compliance writes :

$$\mathbf{\Phi}_K(t-t') = \sum_1^n \left(1 - e^{-\frac{t-t'}{\tau_k}}\right)\mathbf{C}_k^{-1} + \mathbf{C}_0^{-1}$$

where $\mathbf{C}_0$ is the elastic stiffness (order four tensor) and for each $1 \leq k \leq n$, $\mathbf{C}_k$ is the stiffness corresponding to the characteristic time τ_k.

Hence, to define a composite material, it is necessary to describe its microstructure and to depict the behavior of each phase.

1.4. Polymers : Temperature shift and Time shift approach

A time-shift approach is designed to model the aging viscoelastic behavior of the matrix. See Grasley & Lange [54] for a description of this approach, which has been used to model cement paste. Samples are loaded at different times t' elapsed since quenching and the time dependent strains are measured. The obtained strain curves plotted as functions of $log(t-t')$ are identical up to a shift in the horizontal direction, defining a master curve $\mathbf{\Phi}$, so that the aging compliance is written as :

$$\mathbf{J}(t,t') = \mathbf{\Phi}(\xi(t) - \xi(t'))$$

where $\xi(t)$ is a pseudo-time. Struik[15], following Kohlrausch[55], found the Kohlrausch-Williams-Watts (KWW) [56] function

$$\mathbf{\Phi}_{KWW}(t) = \mathbf{J}_0 e^{\left(\frac{t}{\tau_0}\right)^m}$$

where $\mathbf{J}_0$ is an isotropic stiffness tensor and $m = 1/3$ is common to various polymers below the glassy temperature and to metals. This function is also valid for PVC at 63°C [19].

The pseudo time $\xi(t)$ is given by [57] :

$$\xi(t) - \xi(t') = \int_{t'}^{t} \frac{dv}{A(v)}$$

where $A(t)$ is an activity. For instance[54],

$$A(t) = \left(\frac{t}{t_{ref}}\right)^{-\mu} \left(\frac{T(t)}{T_{ref}}\right)^{-\mu_T}$$

where μ is the time shift factor and μ_T is a temperature shift factor. A change of variable $u = \xi(t)$, $\sigma^*(u) = \sigma(t)$ where u is the equivalent time may be performed to turn the aging problem into a non-aging one :

$$\varepsilon(t) = \int_0^{\xi(t)} \mathbf{\Phi}(\xi(t) - v) \frac{d\sigma^*}{du}(v) dv$$

1.5. Identification of the viscoelastic parameters

The identification of the parameters of the constitutive law is performed in two steps. First, the aging parameter μ_{KWW} and the parameters of the KWW function m, τ_0 and $\mathbf{J}_0$ are fitted at once according to the experimental results. Then, to enable 3D numerical computations, a series of Kelvin chain is fitted according to the KWW function.

To perform the first step, the Levenberg-Marquardt algorithm [58, 59] is used, as implemented in the gnuplot software[60]. This algorithm minimizes the scalar

$$\chi^2 = \sum_i \sum_j \left(\frac{\mathbf{\Phi}_{KWW}(\xi(t_{ij}) - \xi(t'_i)) - y_{ij}}{\delta y_{ij}} \right)^2$$

where y_{ij} is the experimental strain measured at time t_{ij} on the sample loaded at time t'_i and δy_{ij} is the standard deviation of y_{ij}. δy_{ij} could be interpreted as an estimation of the error on y_{ij}, or as a weight $w_{ij} = 1/\sqrt{\delta y_{ij}}$. These weights are chosen so that all curves have the same weight and all decades of a given curve have the same weight for fitting. Let N_i be the number of points in a creep curve and N_{ij} be the number of points of that curve between $t_{ij}/\sqrt{10}$ and $\sqrt{10}t_{ij}$. The corresponding weight worths $w_{ij} = 1/(N_{ij}.N_i)$.

The procedure described in the present section was applied to the digitalized experimental results of Struik [15] (Fig. 3)(Tab. 1) and to those of Read et. al. [18]. The obtained results are presented in figure 4 and table 2. Note that the identified values of μ and m are similar to those identified by Read et. al.[18].

For the second step, a series of Kelvin chain $\mathbf{\Phi}_K$ is identified to the master curve $\mathbf{\Phi}_{KWW}$, keeping the same equivalent time $\xi(t)$. Hence, the aging parameter $\mu_K = \mu_{KWW}$ is left unchanged. As performed in the collocation method [61, 62, 63], characteristic times τ_i are chosen as terms of a geometric sequence, with one term per decade, and corresponding Young modulus $\mathbf{E}_i$ are required to be positive. This requirement is sufficient to ensure the thermodynamic correctness of the identified compliance [63]. The KWW function is sampled at equivalent times in a geometric sequence, between half the smallest characteristic time and twice the largest one, so that each decade has the same weight.

For a regular uniaxial loading, the representation of the KWW function by a series of Kelvin chain is accurate as shown in figure 3 and 4. It must be noticed that identifying directly μ and $\mathbf{E}_i$ on the experimental data with the Levenberg-Marquardt algorithm has been tried unsuccessfully.

2. Homogenization of aging viscoelastic materials

In an heterogeneous material, the compliance $\mathbf{J}(x,t,t')$ depends on the spacial position x. Mean-field homogenization schemes and numerical simulations are designed to estimate the overall compliance of the composite material.

2.1. Micromechanical models

To upscale the viscoelastic response of a non-aging viscoelastic material, the Laplace-Carson transform is combined to mean-field homogenization schemes [64, 63]. The Laplace-Carson transform turns a non-aging viscoelastic homogenization problem into a set of elastic homogenization problems parametrized by $p > 0$. The transform of a function $g(t)$ is $\hat{g}(p) = p\int_0^\infty g(t)e^{-pt}dt$ (Appendix A). This transform is still usable in this study since aging is defined as an equivalent time.

Mean field homogenization schemes considered in the present study are the Hashin-Shtrikman lower bound [65] or the Mori-Tanaka scheme [20], as reconsidered by Benveniste [66]. These mean field methods rely on Eshelby's equivalent inclusion theory [67] to estimate the stress concentrations in ellipsoidal inclusions. Weng [68], extending the results of Zhao and Tandon [69], have proven that the effective moduli of the composite containing either aligned or random oriented, identically shaped ellipsoidal inclusions, as estimated by the Mori-Tanaka scheme, have the same expression as those of the Hashin-Shtrikman-Walpole bounds, only with the latter's comparison material identified as the matrix phase and Eshelby's tensor interpreted according to the appropriate inclusion shape. For a given p, the elastic Mori-Tanaka estimate $\mathbf{C}^p_{MT}$ accounts for the volume fraction of inclusions c_i and the distribution of orientations of inclusions $f(\psi)$. It is the solution of equation :

$$c_i \int_\psi f(\psi)(\mathbf{C}^p_{MT} - \mathbf{C}_i(\psi)) : \mathbf{T}^p(\psi)d\psi + (1-c_i)(\mathbf{C}^p_{MT} - \mathbf{C}^p_m) = 0$$

Here, $\mathbf{C}_i(\psi)$ is the elastic stiffness of inclusions having orientation ψ ; $\mathbf{C}_m^p$ is the elastic stiffness of the matrix corresponding to p ; $\mathbf{T}^p(\psi)$ is the strain concentration tensor expressing the strain in the inclusions having orientation ψ as a linear function of the strain at infinity, $\mathbf{C}_m^p$ being the elastic stiffness tensor of the reference material. Tensors $\mathbf{C}_i(\psi)$ and $\mathbf{T}^p(\psi)$ are computed by rotating $\mathbf{C}_i(0)$ and $\mathbf{T}^p(0)$ using Bond transformations [70, 71]. Formula to compute $\mathbf{T}^p(0)$ in the local reference are recalled in references [72, 73, 34].

The average stress in the inclusions of orientation ψ is expressed as a linear function of the overall strain through the localization tensor $\mathbf{B}^p(\psi)$ given by :

$$\mathbf{B}^p(\psi) = \mathbf{C}_i(\psi) : \mathbf{T}^p(\psi) : \left(c_i \int_{\psi'} f(\psi') \mathbf{T}^p(\psi') d\psi' + (1 - c_i)\mathbf{1} \right)^{-1}$$

Once the Laplace-Carson transform is inverted, the Rankine criterion of the average stress in the inclusions of orientation ψ is computed to detect the failure of these inclusions. The Rankine criterion is computed by using the routine `dsyev()` of the LAPACK package [74].

It should be mentioned that many homogenization schemes have recently been adapted by Sanahuja [26] to treat arbitrary aging compliances such as the KWW compliance, or any interpolation of experimental points : instead of using the Laplace-Carson transform, this method operates in the time domain. The expression of the strain localization operator requires computations of Volterra integrals by using trapezoidal rules and inversions of lower triangular per block matrices [75, 76]. Sanahuja's method handles the case of matrix-inclusion composites with spherical inclusions and we are currently investigating its extension to matrix-inclusion composites with ellipsoidal inclusions.

2.2. 3D numerical computations

In the frame of periodic homogenization, the determination of the overall viscoelastic behavior of a periodic microstructure can be obtained by solving the following auxiliary problem on the periodic unit cell V.

$$\begin{array}{rcll} \text{div } \sigma(x,t) & = & 0 & x \in V \\ \varepsilon(x,t) & = & \int_0^t \mathbf{J}(x,t,t') \frac{d\sigma}{dt}(x,t') dt' & x \in V \\ \varepsilon(x,t) & = & E(t) + \nabla^s u(x,t) & x \in V \\ u(x,t) & & \textit{periodic} & x \in \partial V \\ \sigma(x,t) \cdot n(x) & & \textit{anti} - \textit{periodic} & x \in \partial V \end{array}$$

Here $E(t)$ is the time-dependent overall strain, $u(t,x)$ is the displacement field in V,$\nabla^s u(x,t)$ is its symmetric gradient, ∂V is the boundary of V and $n(x)$ is the outer normal to ∂V. Actually, $E(t)$ is the volume average of $\varepsilon(x,t)$ and we denote by $\Sigma(t)$ the volume average of $\sigma(x,t)$.

3D numerical computations have already been performed to upscale mechanical properties of composites in the frame of the periodic homogenization theory. The finite element method or the Fast Fourier Transform (FFT) method [77, 27, 78, 79, 80] are used to solve elastic problems. The Random Sequential Adsorption algorithm [81] is used to generate periodic microstructures[82, 83](Fig. 1b). Overlapping between polyhedral inclusions is prevented thanks to the Gilbert-Johnson-Keerthi distance algorithm [84] as in [85]. The distribution of orientations of fibers is isotropic : the direction of each fiber is randomly picked on the unit sphere. To test if the distribution of the orientations of fibers is isotropic, a 400μm-wide microstructure featuring 1223 fibers is built and chi square tests are performed. Fiber orientations are binned into 20 sectors of equal angle and the estimated number of fibers in each sector ($n_{f,e} = 61, 1$) is compared to the observed ones $n_{f,o}(\theta)$, $\theta \in 1..20$ (Fig. 5). The chi-squared test statistic $\chi^2 = \sum_{\theta=1}^{20}(n_{f,o}(\theta) - n_{f,e})^2/n_{f,e}$ is computed and is found to be 9.7, 14.5 and 18.6 depending on the axis chosen to split the sectors (x, y and z). If χ^2 follows a chi-squared distribution of 19 degrees of freedom, there is a 70% probability that χ^2 is lower than 21.7. Hence, the obtained values of χ^2 are not surprising and an isotropic distribution of the orientations of fibers can produce such a set of observations.

The 3D numerical method used in the present article is the one designed by Šmilauer and Bažant [27] developed for cementitious materials. This method which relies on the exponential algorithm [86, 87, 88] is a time-iteration procedure to solve the viscoelastic problem for the case of steady loads. It features an integration of the constitutive equations on each time step assuming a constant stress rate, to enable the time step to grow exponentially when performing a relaxation (or creep) simulation. This assumption is adapted to treat the case of a time-shift aging compliance based on a series of Kelvin chains, which writes:

$$\boldsymbol{J}(t,t') = \sum_{k\geq 1}\left(1 - e^{-\frac{t^{\mu+1}-t'^{\mu+1}}{(\mu+1)t_{ref}^{\mu}\tau_k}}\right)\boldsymbol{C}_k^{-1} + \boldsymbol{C}_0^{-1}$$

The internal variables are:

$$\gamma_k(t) = \int_0^t \frac{t^{\mu}}{\tau_k t_{ref}^{\mu}} e^{-\frac{t^{\mu+1}-t'^{\mu+1}}{(\mu+1)t_{ref}^{\mu}\tau_k}}\boldsymbol{C}_k^{-1}\dot{\sigma}(t')dt'$$

and the evolution equations write:

$$\begin{aligned}\dot{\varepsilon}(t) &= \boldsymbol{C}_0^{-1}\dot{\sigma}(t) + \sum_{k\geq 1}\gamma_k \\ \dot{\gamma}_k(t) + \frac{t^{\mu}}{\tau_k t_{ref}^{\mu}}\gamma_k(t) - \frac{\mu}{t}\gamma_k(t) &= \frac{t^{\mu}}{\tau_k t_{ref}^{\mu}}\boldsymbol{C}_k^{-1}\dot{\sigma}(t)\end{aligned}$$

The constitutive equation is integrated on the time step $[t_i; t_{i+1}]$ under the following assumption:

$$\sigma(t) = \sigma(t_i) + \Delta\sigma \frac{t^{\mu+1} - t_i^{\mu+1}}{t_{i+1}^{\mu+1} - t_i^{\mu+1}}$$

where μ is the aging parameter (Appendix B). This assumption is unchanged for non-aging material ($\mu = 0$), for which the stress varies linearly on the time step.

The exponential algorithm has been recently combined with the FFT algorithm as solver for the unit cell tangent problem [27, 78]. The FFT algorithm requires the microstructure to be discretized on a regular grid. Consequently, issues regarding the automatic generation of high-quality adapted meshes for the finite element method are avoided.

The strain ε triggered by a periodic polarization field τ in an homogeneous material of stiffness $\mathbf{C}_0^*$, submitted to the average strain E is given by the Lippman-Schwinger equation:

$$\varepsilon = E - \mathbf{\Gamma}_0^* * \tau$$

where $\mathbf{\Gamma}_0^*$ is a Green operator. The convolution of $\mathbf{\Gamma}_0^*$ and τ is computed in the frequency domain thanks to the FFT. The polarity tensor τ is chosen so as to account for the heterogeneity of the considered material $\mathbf{C}(x)$:

$$\tau(x) = (\mathbf{C}(x) - \mathbf{C}_0^*) : \varepsilon(x)$$

The strain field must satisfy the following equation:

$$\varepsilon = E - \mathbf{\Gamma}_0^* * ((\mathbf{C} - \mathbf{C}_0^*) : \varepsilon)$$

This equation is solved by a fixed point algorithm [77](Appendix C).

Although this 3D numerical method can treat large and complex microstructures, it requires large amount of memory and time. The implementation used in this article is parallel so as to be ran on clusters [85].

Such 3D computations may deliver more precise estimates of the overall behavior than mean-field methods since they rely on an accurate description of the microstructure. Moreover, a distribution of stress concentrations per phase may be retrieved. Large scale computations are required to match both the need for a Representative Elementary Volume and the need for a precise description of the microstructural details.

A careful assessment of the quality of 3D numerical computations is performed in the next section.

2.2.1. Convergence study

Time discretization

To assess the accuracy of the integration of the constitutive law on the time step, the response of the matrix to an uniaxial relaxation test $\sigma_{num}(t)$ is numerically computed for different rate of growth of the time step $b = (t_{i+1} - t_i)/(t_i - t_{i-1})$ (Fig. 6). The Laplace-Carson transform provides a reference $\sigma_{LC}(t)$ to compute a relative error $(\sigma_{num}(t) - \sigma_{LC}(t))/\sigma_{LC}(t)$. This relative error is found to be very small, as long as the rate of growth remains limited. A rate of growth of 1.118 is set for further computations. Approximately 180 time steps are needed to compute the response between $t_1 - t_0 = 10^{-3}$ s and $t - t_0$=50 days, the materials being loaded $t_0 = 10$ days after quenching.

Space discretization

The FFT algorithm solves the tangent elastic problem on each time step. To perform fast Fourier transform, strain $\varepsilon(t, x)$, stress $\sigma(t, x)$ and internal variables are stored on a regular grid of $N \times N \times N$ points, where N is called the grid size. The microstructure is also discretized on a regular grid (Fig. 7). Hence, some information about the microstructure is lost, which could trigger an error due to discretization. In order to lower the error, for each voxel, a local volume fraction based on 64 sensing points is computed and a Reuss-like constitutive law is computed and assigned to each voxel [85]. Therefore, the microstructure is made of black voxels (pure matrix), white voxels (pure inclusions) and gray voxels (composite).

To estimate the error due to space discretization, a given microstructure, $l = 133\mu$m in length, is discretized at different grid step (Fig. 7,9) and the response to a shear creep test are computed. Grid sizes N and numerical performances are provided in table 3: the largest grid is $N = 648$ and the numerical shear creep test took less than a day thanks to parallel computing. The probability distribution function of the Von Mises stress depicts the magnitude of stress concentrations within the microstructure and it is a matter of concern for further durability assessment, especially if non-linear phenomenon were to be considered. The estimation of this distribution depends on the grid size N and it becomes more accurate as the grid size increases (Fig. 9).

Representative Elementary Volume

It is well-known that the asymptotic overall response should not depend on the generated sample neither on the size of the unit cell l which must be large enough to be representative of the microstructure ([89, 90] among others). A size of the unit cell $l = 200\mu$m of two times the length of the fibers is chosen and the unit cell is discretized on a $N = 384$ grid so that the error due to representativity is of the same magnitude as the error due to discretization. To assess the error due to representativity, different sizes of the unit cell l and nine samples of each size were generated (Fig. 10a). Since the distribution of orientations of fibers is chosen as uniform, the overall behavior is expected to be isotropic. For a given size, numerical hydrostatic and shear creep tests are performed to

estimate the average of overall responses and the relative standard deviation of these responses. As l increases, the average of nine overall responses does not change much and the standard deviation of these nine responses decreases(Fig. 10b). The standard deviation of the elastic strain of an hydrostatic test is much lower that the standard deviation of the elastic strain of a shear test, as if the representative elementary volume for the shear test were larger than the one for a hydrostatic test. Two reasons could explain such a discrepancy. On the one hand, the Poisson's ratio of the matrix, the soft phase, is twice as large as the one of the fibers. Hence the ratio of bulk moduli is lower than the ratio of shear moduli: the contrast between phases is larger if shear is considered. On the other hand, when an hydrostatic test is performed, all fibers are acting as reinforcements, independently of their orientation. In the shear test σ_{xy}, fibers aligned along z exhibit lower stress concentrations than fibers in the xy plane. Hence, the overall result might be more sensible to the set of orientations of fibers in the cubic cell.

It should be mentioned that the relative standard deviations are lower than the error due to space discretization (5%): the later may be considered as a bias. The average overall results are stable because the grid size N was proportional to l. Relative standard deviations increase during numerical creep tests, as the contrast between tangent stiffnesses of inclusions and matrix increases. The estimate of the probability distribution function of the Von Mises stress depends slightly on l: it gets smoother as l increases (Fig. 11).

3. Results and discussions

3.1. Overall properties

The results of the Hashin-Shtrikman lower bound in the Laplace-Carson space are first compared to 3D numerical results featuring spherical inclusions or short cylindrical inclusions in figure 12, the volume fraction of inclusions being 20%. The length of short cylindrical inclusions is equal to their diameter. For the hydrostatic creep test, the numerical time-dependent strains are close to the one estimated by the Hashin-Shtrikman bound, while a discrepancy is to be noticed for the shear creep test. This discrepancy may be attributed to the contrast between the mechanical behavior of phases: the elastic bulk modulus of glass fibers is 8.1 times the one of PVC and the shear modulus of glass fiber is 28.3 times the one of PVC. During viscoelastic 3D computations, this contrast changes at each time step: the ratio of bulk moduli changes from 8.1 to 10.9, while the ratio of shear moduli changes from 28.3 to 36.5. For the shear creep test, the time-dependent strains depends slightly on the shape of inclusions: short cylindrical inclusions induce a small decrease of the time-dependent strain compared to spherical inclusions.

For 100μm-long fibers, the aspect ratio of fibers induces a larger difference between the behavior estimated by the Hashin-Shtrikman bound and the one estimated by 3D numerical computations. The Hashin-Shtrikman bound does not take account of the shape of inclusions. Hence, the shape of inclusions is a good candidate to explain the difference between the overall strain estimated by the Hashin-Shtrikman bound and the one estimated by numerical simulations. Indeed, the Mori-Tanaka estimate, with an aspect ratio identical to the one of the fibers (10), is very close to the result of numerical simulations (Fig. 13).

A parametric study of the influence of the volume fraction of inclusions (Fig. 14) and of the aspect ratio (Fig. 13) of fibers is performed. The range of aspect ratio and volume fraction is limited by the Random Sequential Algorithm applied to build the unit cells. Mori-Tanaka estimates are close to numerical results, as long as the aspect ratio is lower than 10 and the volume fraction lower than 20%.

3.2. Stress concentrations

The 3D numerical computations produce estimates of stress concentrations (Fig. 15). Hence, it is possible to display the Von Mises stress within the matrix and the Rankine criteria within the fibers. It is shown here that there is little difference between the instantaneous Von Mises stress and the one 50 days after loading (Fig. 16). The Von Mises stress slightly decreases far from the fibers and increases close to the fibers. The fibers already bear much of the loading right after loading time and it increases slightly with time. It is clearly visible on the probability distribution function of the Rankine criteria during an hydrostatic creep test. Since no orientation of fibers is favored by this loading, stress concentrations in fibers trigger a rise on the probability distribution function and this rise shifts toward larger stress concentrations during the creep test. On the contrary, in case of a shear creep test, there is no rise on the probability distribution function and this distribution does not change over time elapsed since loading. A small increase of large stress concentrations in the matrix is visible on the probability distribution function of the Von Mises stress in the matrix.

In case of an hydrostatic loading, the Mori-Tanaka model expects the Rankine criteria to be equal in all fibers. Yet, the numerical computations exhibit a wide distribution of the Rankine criteria in the fibers (Fig. 16). Though the overall strains predicted by these models are similar, stress concentrations may be different.

3.3. Prediction of lifetime of the material under tensile stress

A tensile stress σ_l is applied to the material and both the overall strain and the Rankine criteria in fibers are estimated. According to the Mori-Tanaka estimate of stress concentrations, the fibers aligned with the direction of loading feature the largest Rankine criterion $\sigma_R(t)$ and they are expected to fail first [24]. The

Von Mises stress in these fibers increases with time elapsed since loading, which explains the delayed rupture of the material. Since the model remains in the range of linear viscoelasticity, a single run is necessary to define a ratio $r(t) = \sigma_R(t)/\sigma_l$ between the Rankine criterion and the level of loading and this ratio increases with time. A critical stress of fibers σ_c is introduced and the lifetime t_l under load $\sigma_{l'}$ is such that $r(t_l)\sigma_{l'} = \sigma_c = r(0)\sigma_0$, where σ_0 is the tensile strength of the material. The Mori-Tanaka estimate predicts a decrease of the lifetime as the creep load increases (Fig. 17), which is consistent with experiments. The estimated strain at failure is almost uniform in time. The critical stress of fibers σ_c^{MT} is set to 2.4GPa to match the experimental instantaneous tensile strength of the material.

3D numerical computations also deliver an estimate of the Rankine criteria in the microstructure. As in [91], the failure of the specimen is expected to occur when the Rankine criterion is above σ_c^{3D} in a volume fraction of fiber equal to c_R^{3D}. Note that, using the maximum value of the criterion in all the specimen ($c_R^{3D} \to 0$) would make the result too volatile and using a large c_R^{3D} would not be realistic. The volume fraction c_R^{3D} being set, σ_c^{3D} is adjusted to match the overall instantaneous tensile strength of the material (Fig. 18). If σ_c^{3D} is set to 2.4GPa, a c_R^{3D} of 0.5% is required to match the instantaneous tensile strength. Yet, for a given creep load, the numerical simulations predict a shorter lifetime than the Mori-Tanaka estimate using the same value $\sigma_c^{MT} = 2.4$GPa. Indeed, the fact that the Mori-Tanaka estimate is based on the Rankine criterion of the average stress for a given direction is a reason of this discrepancy: the 3D numerical estimate accounts for the heterogeneity of the stress field in the fibers. A larger c_R^{3D} mitigates the effect of stress concentrations: for $c_R^{3D} = 2\%$ and $\sigma_c^{3D} = 1.2$GPa, the numerical estimate of creep failure is close to one obtained by the Mori-Tanaka scheme, which requires the Rankine criteria of the average stress in fiber parallel to the loading direction to be $\sigma_c^{MT} = 2.4$GPa. Hence, the Mori-Tanaka model is a practical tool to estimate the creep failure of the composite material.

Aging affects the Mori-Tanaka estimate of creep failure in the same way it changes the creep strain: the composite material is aging viscoelastic and can be modeled by the time-shift method, the μ parameter being the one identified on the creep tests of the polymer matrix. The lifetime of the pipe is expected to increase if it is loaded later than 21 days after quenching.

A parametric study of the effect of the volume fraction of fibers and fiber length on the Mori-Tanaka estimate of creep failure is performed (Fig. 19). The tensile strength of the glass fibers is set at $\sigma_c^{MT} = 2.4$GPa and the composite material is loaded at 21 days. A raise of the volume fraction of inclusions induces a raise of the tensile strength of the material and its lifetime. If the fibers are more than 1mm long, the fiber length has little influence on the tensile strength

and creep failure. On the contrary, fibers smaller than 300μm may enable larger tensile strengths and improve durability. In this case, larger strains may appear and the durability might be limited by the mechanical properties of the polymer or by the quality of bonding between fibers and polymers, which are not taken account of in the present study.

3.4. Discussion

The model presented in this article has several limitations compared to other models in the literature. It has been mentioned that it does not account for the statistical variability of the strength of fibers [44, 45] and the effect of moisture on the stress corrosion cracking of glass fibers [46, 51] is ignored. Moreover, this model does not describe the progressive rupture of the fibers until the final rupture of the specimen: models have been designed to investigate damage phenomena [23, 24], by including damage in the matrix or debonding. Regarding uniaxial composites, the shear lag model [92, 93] may be extended to viscous matrices [94, 95] to investigate the load transfer after the breakage of a fiber and explain delayed failure of the composite under constant load. The present study remains in the range of the linear strain theory, which is not seen as a limitation, since the experimental strain at failure is less than 2% [9]. Numerical strain at failure reaches 7% if 100μm-long fibers are considered. In such cases, it is likely that either damage in the matrix or fiber debonding would have to be considered, as performed in [96].

Regarding the ability of the Mori-Tanaka estimate to depict the effect of short fibers on creep strains, our results is limited to volume fraction of fibers lower than 20%. In this range, the Mori-Tanaka estimate is expected to be close to the one of Lielen [32]. Hence, our results comply with existing results in the range of elasticity [28, 29, 30].

The fiber failure may be defined by using the axial stress [97, 24]. It may be the case in the shear-lag model, where fibers may be considered as springs [93]. The use of the Rankine criteria should deliver comparable results: it has been observed on our 3D computational results that the maximal principal stress is almost parallel to the axis of the fiber during an uniaxial tensile creep test (Fig. 20).

Conclusion

The results of full field computations and mean-field homogenization methods have been compared in the range of viscoelasticity, on a fiber reinforced polymer. If the volume fraction of fibers is lower than 20% and the behavior of the matrix similar to the one of PVC, combining the Laplace-Carson transform on the equivalent time and the Mori-Tanaka scheme was sufficient to produce an accurate estimate of the overall time-dependent strain.

3D numerical simulations produce estimates of stress concentrations. It has been shown that stress concentrations may change during a creep test. In particular, the fibers bear an increasing part of the load: an increase of Rankine criteria in fibers is clearly visible during an hydrostatic creep test. The Von Mises stress may slightly increase in the viscoelastic matrix as well, on the high side of the Von Mises stress probability distribution function, even if the most part of the matrix is relaxing. Such a feature might trigger a delayed damage of the material. As 3D numerical computations and the Mori-Tanaka scheme lead to similar estimate of creep failure based on the Rankine criteria, the Mori-Tanaka model remains an efficient and practical tool to estimate the creep failure of the composite material.

Regarding 3D numerical simulations, further developments are necessary to properly handle the case of long fibers such as the one used in the automotive industry or pipes.

Appendix A. Hashin-Shtrikman bound and Laplace-Carson transform

Appendix A.1. The correspondence principle

The non-aging linear viscoelastic problem corresponds to elastic problems thank to the Laplace-Carson transform. The transform of a function $g(t)$ is $\hat{g}(p) = p\int_0^\infty g(t)e^{-pt}dt$. The transform of its derivative $\dot{g}(t)$ is $\hat{\dot{g}}(p) = p\hat{g}(p) - p.g(0)$.

Elastic inclusions (volume fraction f_i) are embedded in a viscoelastic matrix modeled by a single Kelvin chain. The relaxation problem reads:

$$\begin{array}{rcll} \text{div}\,\sigma(x,t) & = & 0 & x \in V \\ \sigma(x,t) & = & C_i\varepsilon(x,t) & x \in \text{inclusions} \\ \sigma(x,t) & = & C_m\varepsilon(x,t) + \tau C_m\dot{\varepsilon}(x,t) & x \in \text{matrix} \\ \varepsilon(x,t) & = & E(t) + \nabla^s u(x,t) & x \in V \\ u(x,t) & & periodic & x \in \partial V \\ \sigma(x,t)\cdot n(x) & & anti-periodic & x \in \partial V \end{array}$$

In the Laplace-Carson space, for each p, this set of equation corresponds to the elastic problem:

$$\begin{array}{rcll} \text{div}\,(\hat{\sigma}(x,p)) & = & 0 & x \in V \\ \hat{\sigma}(x,p) & = & C_i\hat{\varepsilon}(p) & x \in \text{inclusions} \\ \hat{\sigma}(p) & = & (1+p\tau)C_m\hat{\varepsilon}(x,p) & x \in \text{matrix} \\ \hat{\varepsilon}(x,p) & = & E(p) + \nabla^s\hat{u}(x,p) & x \in V \\ \hat{u}(x,p) & & periodic & x \in \partial V \\ \hat{\sigma}(x,p)\cdot n(x) & & anti-periodic & x \in \partial V \end{array}$$

The Hashin-Shtrikman bound is an analytical model which provides estimates of the macroscopic response of the elastic material.

$$< \hat{\sigma}(p) >= \hat{C_{HS}}(p) < \hat{\varepsilon}(p) >= \hat{C_{HS}}(p)E$$

$\hat{C_{HS-}}(p)$ is isotropic and its bulk modulus and shear modulus are:

$$\begin{aligned} K_m(p) &= (1+p\tau)K_m \\ \mu_m(p) &= (1+p\tau)\mu_m \\ K_{HS-}(p) &= K_m(p) + \frac{f_i}{\frac{1}{K_i-K_m(p)}+\frac{3(1-f_i)}{3K_m(p)+4\mu_m(p)}} \\ \mu_{HS-}(p) &= \mu_m(p) + \frac{f_i}{\frac{1}{\mu_i-\mu_m(p)}+\frac{6(K_m(p)+2\mu_m(p))(1-f_i)}{5\mu_m(p)(3K_m(p)+4\mu_m(p))}} \end{aligned}$$

The Laplace-Carson transform of the macroscopic stress $<\hat{\sigma}>(p)$ is computed and the last stage is inverting this transform.

Appendix A.2. Inverting the Laplace-Carson transform

Lots of methods are available to invert the Laplace-Carson transform. In the present study, the Gaver-Stehfest formula [98] has been used:

$$g(t,M) = \sum_{k=1}^{2M} \frac{\xi_k}{k} \hat{g}(\frac{k\ln(2)}{t})$$

and

$$\xi_k = (-1)^{M+k} \sum_{j=E(\frac{k+1}{2})}^{min(k,M)} \frac{j^{M+1}}{M!} \binom{M}{j} \binom{2j}{j} \binom{j}{k-j}$$

Computing the binomial coefficients requires high precision and the long double type (IEEE 754, decimal on 128 bits) provided it. If M is too low, the formula lacks precision [99]. If M is too large, small errors on $\hat{g}(\frac{k\ln(2)}{t})$ may trigger large errors on the outcome. M is set to 7.

Therefore, to estimate the response at time t, about 14 elastic computations are required. The Gaver-Stehfest formula does not seem to be practical for FEM since it lacks stability or precision. It is suitable as long as the numerical error in the Laplace-Carson space remains very low. This formula is useful when the Hashin-Shtrikman analytical formula or self-consistent estimate are computed in the Laplace-Carson space.

Appendix B. Integration on the time step for the exponential algorithm

The strain rate writes:

$$\dot{\varepsilon}(t) = \boldsymbol{C}_0^{-1}\dot{\sigma}(t) + \int_0^t \sum_{k\geq 1} \frac{t^\mu}{\tau_k t_{ref}^\mu} e^{-\frac{t^{\mu+1}-t'^{\mu+1}}{(\mu+1)t_{ref}^\mu \tau_k}} \boldsymbol{C}_k^{-1}\dot{\sigma}(t')dt'$$

The internal variables are:

$$\gamma_k(t) = \int_0^t \frac{t^\mu}{\tau_k t_{ref}^\mu} e^{-\frac{t^{\mu+1}-t'^{\mu+1}}{(\mu+1)t_{ref}^\mu \tau_k}} \boldsymbol{C}_k^{-1} \dot{\sigma}(t') dt'$$

and:

$$\begin{aligned} \dot{\varepsilon}(t) &= \boldsymbol{C}_0^{-1}\dot{\sigma}(t) + \textstyle\sum_{k\geq 1}\gamma_k \\ \dot{\gamma}_k(t) + \frac{t^\mu}{\tau_k t_{ref}^\mu}\gamma_k(t) - \frac{\mu}{t}\gamma_k(t) &= \frac{t^\mu}{\tau_k t_{ref}^\mu}\boldsymbol{C}_k^{-1}\dot{\sigma}(t) \end{aligned}$$

The constitutive law is integrated on the time step $[t_i, t_{i+1}]$ under the following assumption:

$$\sigma(t) = \sigma(t_i) + \Delta\sigma \frac{t^{\mu+1} - t_i^{\mu+1}}{t_{i+1}^{\mu+1} - t_i^{\mu+1}}$$

This choice for $\sigma(t)$ enables to solve the evolution of internal variables through a variation of parameter. The solution for a constant stress $\dot{\gamma}_k(t) + \frac{t^\mu}{\tau_k t_{ref}^\mu}\gamma_k(t) - \frac{\mu}{t}\gamma_k(t) = 0$ writes:

$$\gamma_k(t) = C t^\mu e^{-\frac{t^{\mu+1}-t_i^{\mu+1}}{(\mu+1)t_{ref}^\mu \tau_k}}$$

The assumption on $\sigma(t)$ is used:

$$\begin{aligned} \dot{C} &= \frac{t^\mu}{\tau_k t_{ref}^\mu}\frac{\mu+1}{t_{i+1}^{\mu+1}-t_i^{\mu+1}} e^{\frac{t^{\mu+1}-t_i^{\mu+1}}{(\mu+1)t_{ref}^\mu \tau_k}} \boldsymbol{C}_k^{-1}\Delta\sigma \\ C &= \frac{\mu+1}{t_{i+1}^{\mu+1}-t_i^{\mu+1}} e^{\frac{t^{\mu+1}-t_i^{\mu+1}}{(\mu+1)t_{ref}^\mu \tau_k}} \boldsymbol{C}_k^{-1}\Delta\sigma + D \end{aligned}$$

Hence:

$$\begin{aligned} \gamma_k(t) &= \frac{(\mu+1)t^\mu}{t_{i+1}^{\mu+1}-t_i^{\mu+1}}\boldsymbol{C}_k^{-1}\Delta\sigma + Dt^\mu e^{-\frac{t^{\mu+1}-t_i^{\mu+1}}{(\mu+1)t_{ref}^\mu \tau_k}} \\ \gamma_k(t) &= \frac{(\mu+1)t^\mu}{t_{i+1}^{\mu+1}-t_i^{\mu+1}}\left(1 - e^{-\frac{t^{\mu+1}-t_i^{\mu+1}}{(\mu+1)t_{ref}^\mu \tau_k}}\right)\boldsymbol{C}_k^{-1}\Delta\sigma + \gamma_{k,t_i}\frac{t^\mu}{t_i^\mu} e^{-\frac{t^{\mu+1}-t_i^{\mu+1}}{(\mu+1)t_{ref}^\mu \tau_k}} \\ \gamma_{k,i+1} &= \frac{(\mu+1)t_{i+1}^\mu}{t_{i+1}^{\mu+1}-t_i^{\mu+1}}\left(1 - e^{-\frac{t_{i+1}^{\mu+1}-t_i^{\mu+1}}{(\mu+1)t_{ref}^\mu \tau_k}}\right)\boldsymbol{C}_k^{-1}\Delta\sigma + \gamma_{k,t_i}\frac{t_{i+1}^\mu}{t_i^\mu} e^{-\frac{t_{i+1}^{\mu+1}-t_i^{\mu+1}}{(\mu+1)t_{ref}^\mu \tau_k}} \end{aligned}$$

The strain must be computed:

$$\begin{aligned} \dot{\varepsilon}(t) &= \boldsymbol{C}_0^{-1}\dot{\sigma}(t) + \textstyle\sum_{k\geq 1}\gamma_k(t) \\ \Delta\varepsilon &= \int_{t_i}^{t_{i+1}} \left(\boldsymbol{C}_0^{-1}\dot{\sigma}(t') + \textstyle\sum_{k\geq 1}\gamma_k(t')\right) dt' \end{aligned}$$

The first part, $\boldsymbol{C}_0^{-1}\dot{\sigma}(t')$ writes:

$$\Delta\varepsilon_0 = \boldsymbol{C}_0^{-1}\Delta\sigma$$

The part coming from the internal variables writes:

$$\Delta\varepsilon_k = \left(1 - \frac{(\mu+1)t_{ref}^{\mu}\tau_k}{t_{i+1}^{\mu+1} - t_i^{\mu+1}}\left(1 - e^{-\frac{t_{i+1}^{\mu+1} - t_i^{\mu+1}}{(\mu+1)t_{ref}^{\mu}\tau_k}}\right)\right)\boldsymbol{C}_k^{-1}\Delta\sigma + \frac{t_{ref}^{\mu}\tau_k}{t_i^{\mu}}\left(1 - e^{-\frac{t_{i+1}^{\mu+1} - t_i^{\mu+1}}{(\mu+1)t_{ref}^{\mu}\tau_k}}\right)\gamma_{k,t_i}$$

The sum of these parts is $\Delta\varepsilon$. This defines the tangent elastic problem.

Appendix C. FFT solvers

The basic FFT algorithm (Alg. 1) is the one of Moulinec and Suquet as described in [77]. The accelerated FFT algorithm (Alg. 2) is the one of Eyre and Milton [100]. These algorithms are particular cases of the polarization-based scheme [101, 102]. The error on equilibrium $error_{eq}$ and $\Gamma^0(\xi)$ are computed as described in reference [77]. If the loading is a macroscopic stress Σ instead of a macroscopic strain E, the macroscopic strain E^i is modified at each time step as $E^i = C_0(\Sigma - \langle\sigma^i\rangle) + \langle\varepsilon^i\rangle$, where $\langle\sigma^i\rangle$ denotes the volume average of σ^i. In this case, the error on boundary condition is modified as $error_{bc} =< \sigma^i > -\Sigma$ [77].

Algorithm 1 Basic FFT scheme

Initial strain field $\varepsilon^0(x)$ and prestress $\sigma_0(x)$ are provided
Initial strain field $\hat{\varepsilon}^{-1}(\xi)$ is set
while $error_{eq} > 10^{-7} \times error_{eq,0}$ **do**
  for $x \in$ points **do**
    $\sigma^i(x) \leftarrow C(x)\varepsilon^i(x) + \sigma_0(x)$
  end for
  $\hat{\sigma}^i \leftarrow \mathbf{FFT}(\sigma)$
  Compute error on equilibrium $error_{eq}$
  for $\xi \in$ frequencies **do**
    $\hat{\varepsilon}(\xi)^{i+1} \leftarrow \hat{\varepsilon}(\xi)^i - \Gamma^0(\xi) : \hat{\sigma}^i(\xi)$
  end for
  $\hat{\varepsilon}(0)^{i+1} \leftarrow E$
  $\varepsilon^{i+1} \leftarrow \mathbf{FFT}^{-1}(\hat{\varepsilon}^{i+1})$
end while

[1] E. B. Rabinovitch, J. W. Summers, The effect of physical aging on properties of rigid polyvinyl chloride, Journal of Vinyl Technology 14 (3) (1992) 126–130. doi:10.1002/vnl.730140303.
URL http://dx.doi.org/10.1002/vnl.730140303

Algorithm 2 Accelerated FFT scheme

Initial strain field $\varepsilon^0(x)$ and prestress σ_0 are provided
Initial strain field $\hat{\varepsilon}^{-1}(\xi)$ is set
while $error_{eq} > 10^{-7} \times error_{eq,0}$or $error_{bc} > 10^{-7} \times error_{bc,0}$ or $error_{comp} > 10^{-7}$ **do**
  $\sigma^i(x) \leftarrow C(x)e^i(x) + \sigma_0$
  if $i\%5 == 0$ **then**
    $\hat{\sigma}^i \leftarrow \mathbf{FFT}(\sigma)$
    Compute error on equilibrium $error_{eq}$
  end if
  for $x \in$ points **do**
    $\tau(x) \leftarrow (C(x) - C_0)e^i(x) + \sigma_0(x)$
  end for
  $\hat{\tau} \leftarrow \mathbf{FFT}(\tau)$
  for $\xi \in$ frequencies **do**
    $\hat{e_b}(\xi) \leftarrow -2\Gamma^0(\xi) : \hat{\tau}(\xi)$
  end for
  $\hat{e_b}(0) \leftarrow 2E$
  $e_b \leftarrow \mathbf{FFT}^{-1}(\hat{e_b})$
  $e^{i+1}(x) \leftarrow (C(x) + C_0)^{-1} : (\tau(x) + C_0 : e_b(x) - \sigma_0(x))$
  Error on boundary conditions: $error_{bc} \leftarrow < e^{i+1} > -E$
  Error on compatibility: $error_{comp} \leftarrow \frac{||e^{i+1} - e_b||_2}{||e^{i+1}||_2}$
end while

[2] PlasticsEurope, Plastics - the facts 2013 an analysis of european latest plastics production, demand and waste data, Tech. rep., PlasticsEurope, Association of Plastics Manufacturers (2013).
URL http://www.plasticseurope.org/documents/document/20131014095824-final_plastics_the_facts_2013_published_october2013.pdf

[3] D. Rahrig, Glass fiber reinforced vinyl chloride polymer products and process for their preparation, uS Patent 4,536,360 (Aug. 20 1985).
URL http://www.google.com/patents/US4536360

[4] P. Kinson, E. Faber, Compositions de polychlorure de vinyle renforcée par des fibres de verre avec stabilité dimensionnelle et résistance à la traction, eP Patent 0,313,003 (May 20 1992).
URL http://www.google.com.ar/patents/EP0313003B1?cl=fr

[5] F. O'brien-Bernini, D. Vermilion, S. Schweiger, B. Guhde, W. Graham, G. Walrath, L. Morris, Wet use chopped strand glass as reinforcement in extruded products, wO Patent App. PCT/US2005/040,810 (May 26 2006).
URL http://www.google.com.ar/patents/WO2006055398A1?cl=en

[6] S. Tungjitpornkull, N. Sombatsompop, Processing technique and fiber orientation angle affecting the mechanical properties of e-glass fiber reinforced wood/PVC composites, Journal of Materials Processing Technology 209 (6) (2009) 3079 – 3088. doi:http://dx.doi.org/10.1016/j.jmatprotec.2008.07.021.
URL http://www.sciencedirect.com/science/article/pii/S0924013608005736

[7] J. Hohe, C. Beckmann, H. Paul, Modeling of uncertainties in long fiber reinforced thermoplastics, Materials & Design 66, Part B (0) (2015) 390 – 399, lightweight Materials and Structural Solutions for Transport Applications. doi:http://dx.doi.org/10.1016/j.matdes.2014.05.067.
URL http://www.sciencedirect.com/science/article/pii/S0261306914004440

[8] J. Breen, A. H. in't Veld, Expected lifetime of existing PVC water systems ; summary, Tech. Rep. MT-RAP-06-18693/mso, TNO Science and Industry (2006).
URL http://www.teppfa.com/pdf/CivilsLifetimeofPVCpipes1.pdf

[9] R. M. Guedes, A. Sá, H. Faria, On the prediction of long-term creep-failure of GRP pipes in aqueous environment, Polymer Composites 31 (6) (2010) 1047–1055. doi:10.1002/pc.20891.
URL http://dx.doi.org/10.1002/pc.20891

[10] J. D. Diniz Melo, F. Levy Neto, G. de Araujo Barros, F. N. de Almeida Mesquita, Mechanical behavior of GRP pressure pipes with addition of quartz sand filler, Journal of Composite Materials 45 (6) (2011) 717–726. arXiv:http://jcm.sagepub.com/content/45/6/717.full.pdf+html, doi:10.1177/0021998310385593.
URL http://jcm.sagepub.com/content/45/6/717.abstract

[11] R. Rafiee, F. Reshadi, Simulation of functional failure in GRP mortar pipes, Composite Structures 113 (0) (2014) 155 – 163. doi:http://dx.doi.org/10.1016/j.compstruct.2014.03.024.
URL http://www.sciencedirect.com/science/article/pii/S0263822314001275

[12] AFNOR, Determination du taux de fluage pour les tubes en matières thermoplastiques, Tech. Rep. NF EN ISO 9967:2007, Norme ISO (2007).

[13] ASTM, Standard practice for obtaining hydrostatic or pressure design basis for fiberglass (glass-fiber-reinforced thermosetting-resin) pipe and fittings, Tech. Rep. ASTM Standard D2992 -12, ASTM (2012). doi:10.1520/D2992-12.

[14] R. Guedes, Analysis of a delayed fracture criterion for lifetime prediction of viscoelastic polymer materials, Mechanics of Time-Dependent Materials 16 (3) (2012) 307–316. doi:10.1007/s11043-011-9163-8.
URL http://dx.doi.org/10.1007/s11043-011-9163-8

[15] L. C. E. Struik, Physical aging in amorphous polymers and other materials / L. C. E. Struik, Elsevier Scientific Pub. Co. ; distributors for the U.S. and Canada, Elsevier North-Holland Amsterdam ; New York : New York, 1978.

[16] J. Sullivan, Creep and physical aging of composites, Composites Science and Technology 39 (3) (1990) 207 – 232. doi:http://dx.doi.org/10.1016/0266-3538(90)90042-4.
URL http://www.sciencedirect.com/science/article/pii/0266353890900424

[17] G. M. Odegard, A. Bandyopadhyay, Physical aging of epoxy polymers and their composites, Journal of Polymer Science Part B: Polymer Physics 49 (24) (2011) 1695–1716. doi:10.1002/polb.22384.
URL http://dx.doi.org/10.1002/polb.22384

[18] B. Read, G. Dean, P. Tomlins, J. Lesniarek-Hamid, Physical ageing and creep in PVC, Polymer 33 (13) (1992) 2689 – 2698. doi:http://dx.doi.org/10.1016/0032-3861(92)90439-4.
URL http://www.sciencedirect.com/science/article/pii/0032386192904394

[19] Z.-h. Zhou, Y.-l. He, H.-j. Hu, F. Zhao, X.-l. Zhang, Creep performance of PVC aged at temperature relatively close to glass transition temperature, Applied Mathematics and Mechanics 33 (9) (2012) 1129–1136. doi:10.1007/s10483-012-1610-x.
URL http://dx.doi.org/10.1007/s10483-012-1610-x

[20] T. Mori, K. Tanaka, Average stress in matrix and average elastic energy of materials with misfitting inclusions, Acta Metallurgica 21 (5) (1973) 571 – 574. doi:10.1016/0001-6160(73)90064-3.
URL http://www.sciencedirect.com/science/article/pii/0001616073900643

[21] Y. M. Wang, G. J. Weng, The influence of inclusion shape on the overall viscoelastic behavior of composites, Journal of Applied Mechanics 59 (3) (1992) 510–518. doi:10.1115/1.2893753.
URL http://dx.doi.org/10.1115/1.2893753

[22] K. Li, X.-L. Gao, A. K. Roy, Micromechanical modeling of viscoelastic properties of carbon nanotube-reinforced polymer composites, Mechanics of Advanced Materials and Structures 13 (4) (2006) 317–328. arXiv:http://dx.doi.org/10.1080/15376490600583931, doi:10.1080/15376490600583931.
URL http://dx.doi.org/10.1080/15376490600583931

[23] T. Sasayama, T. Okabe, Y. Aoyagi, M. Nishikawa, Prediction of failure properties of injection-molded short glass fiber-reinforced polyamide 6,6, Composites Part A: Applied Science and Manufacturing 52 (0) (2013) 45 – 54. doi:http://dx.doi.org/10.1016/j.compositesa.2013.05.004.
URL http://www.sciencedirect.com/science/article/pii/S1359835X13001383

[24] M. Hashimoto, T. Okabe, T. Sasayama, H. Matsutani, M. Nishikawa, Prediction of tensile strength of discontinuous carbon fiber/polypropylene composite with fiber orientation distribution, Composites Part A: Applied Science and Manufacturing 43 (10) (2012) 1791 – 1799, compTest 2011. doi:http://dx.doi.org/10.1016/j.compositesa.2012.05.006.
URL http://www.sciencedirect.com/science/article/pii/S1359835X12001625

[25] J.-M. Ricaud, R. Masson, Effective properties of linear viscoelastic heterogeneous media: Internal variables formulation and extension to ageing behaviours, International Journal of Solids and Structures 46 (7–8) (2009) 1599 – 1606. doi:10.1016/j.ijsolstr.2008.12.007.
URL http://www.sciencedirect.com/science/article/pii/S0020768308005027

[26] J. Sanahuja, Effective behaviour of ageing linear viscoelastic composites: Homogenization approach, International Journal of Solids and Structures 50 (19) (2013) 2846 – 2856. doi:http://dx.doi.org/10.1016/j.ijsolstr.2013.04.023.
URL http://www.sciencedirect.com/science/article/pii/S0020768313001807

[27] V. Šmilauer, Z. P. Bažant, Identification of viscoelastic C-S-H behavior in mature cement

paste by FFT-based homogenization method, Cement and Concrete Research 40 (2) (2010) 197 – 207. doi:10.1016/j.cemconres.2009.10.003.
URL http://www.sciencedirect.com/science/article/pii/S0008884609002865

[28] C. L. T. III, E. Liang, Stiffness predictions for unidirectional short-fiber composites: Review and evaluation, Composites Science and Technology 59 (5) (1999) 655 – 671. doi:http://dx.doi.org/10.1016/S0266-3538(98)00120-1.
URL http://www.sciencedirect.com/science/article/pii/S0266353898001201

[29] H. Moussaddy, A new definition of the representative volume element in numerical homogenization problems and its application to the performance evaluation of analytical homogenization models, Ph.D. thesis, Ecole Polytechnique de Montréal (2013).

[30] E. Ghossein, M. Lévesque, A comprehensive validation of analytical homogenization models: The case of ellipsoidal particles reinforced composites, Mechanics of Materials 75 (0) (2014) 135 – 150. doi:http://dx.doi.org/10.1016/j.mechmat.2014.03.014.
URL http://www.sciencedirect.com/science/article/pii/S016766361400057X

[31] A. E. Moumen, T. Kanit, A. Imad, H. E. Minor, Effect of reinforcement shape on physical properties and representative volume element of particles-reinforced composites: Statistical and numerical approaches, Mechanics of Materials 83 (0) (2015) 1 – 16. doi:http://dx.doi.org/10.1016/j.mechmat.2014.12.008.
URL http://www.sciencedirect.com/science/article/pii/S016766361400221X

[32] G. Lielens, P. Pirotte, A. Couniot, F. Dupret, R. Keunings, Prediction of thermo-mechanical properties for compression moulded composites, Composites Part A: Applied Science and Manufacturing 29 (1–2) (1998) 63 – 70, selected Papers Presented at the Fourth International Conference on Flow Processes in Composite Material. doi:http://dx.doi.org/10.1016/S1359-835X(97)00039-0.
URL http://www.sciencedirect.com/science/article/pii/S1359835X97000390

[33] N. Lahellec, P. Suquet, Effective behavior of linear viscoelastic composites: A time-integration approach, International Journal of Solids and Structures 44 (2) (2007) 507 – 529. doi:http://dx.doi.org/10.1016/j.ijsolstr.2006.04.038.
URL http://www.sciencedirect.com/science/article/pii/S002076830600148X

[34] O. Pierard, C. González, J. Segurado, J. LLorca, I. Doghri, Micromechanics of elasto-plastic materials reinforced with ellipsoidal inclusions, International Journal of Solids and Structures 44 (21) (2007) 6945 – 6962. doi:http://dx.doi.org/10.1016/j.ijsolstr.2007.03.019.
URL http://www.sciencedirect.com/science/article/pii/S0020768307001473

[35] O. Pierard, J. LLorca, J. Segurado, I. Doghri, Micromechanics of particle-reinforced elasto-viscoplastic composites: Finite element simulations versus affine homogenization, International Journal of Plasticity 23 (6) (2007) 1041 – 1060. doi:http://dx.doi.org/10.1016/j.ijplas.2006.09.003.
URL http://www.sciencedirect.com/science/article/pii/S0749641906001598

[36] F. T. Wallenberger, J. C. Watson, H. Li, Glass fibers, asm handbook, Tech. Rep. 06781G, ASM International (2001).

[37] AGY, High strength glass fibers, Tech. Rep. LIT-2006-111 R2, AGY (2001).

[38] D. Mounier, C. Poilâne, C. Bûcher, P. Picart, Evaluation of transverse elastic properties of fibers used in composite materials by laser resonant ultrasound spectroscopy, in: S. F. d'Acoustique (Ed.), Acoustics 2012, Nantes, France, 2012.
URL https://hal.archives-ouvertes.fr/hal-00811303

[39] E. Haque, Polymer/wucs mat for use in automotive applications, uS Patent 7,279,059 (Oct. 9 2007).
URL http://www.google.com/patents/US7279059

[40] R. Nakano, Use of polyvinyl chlorine resin sheets as flooring material, eP Patent 0,732,354 (Aug. 13 2003).

URL http://www.google.com/patents/EP0732354B1?cl=en

[41] J. Yuan, A. Hiltner, E. Baer, D. Rahrig, The effect of high pressure on the mechanical behavior of short fiber composites, Polymer Engineering & Science 24 (11) (1984) 844–850. doi:10.1002/pen.760241103.
URL http://dx.doi.org/10.1002/pen.760241103

[42] S. Tungjitpornkull, K. Chaochanchaikul, N. Sombatsompop, Mechanical characterization of e-chopped strand glass fiber reinforced wood/PVC composites, Journal of Thermoplastic Composite Materials 20 (6) (2007) 535–550. arXiv:http://jtc.sagepub.com/content/20/6/535.full.pdf+html, doi:10.1177/0892705707084541.
URL http://jtc.sagepub.com/content/20/6/535.abstract

[43] J. H. Phelps, A. I. A. El-Rahman, V. Kunc, C. L. T. III, A model for fiber length attrition in injection-molded long-fiber composites, Composites Part A: Applied Science and Manufacturing 51 (0) (2013) 11 – 21. doi:http://dx.doi.org/10.1016/j.compositesa.2013.04.002.
URL http://www.sciencedirect.com/science/article/pii/S1359835X13001048

[44] T. Chiao, R. Moore, Stress-rupture of s-glass epoxy multifilament strands, Journal of Composite Materials 5 (1) (1971) 2–11. arXiv:http://jcm.sagepub.com/content/5/1/2.full.pdf+html, doi:10.1177/002199837100500101.
URL http://jcm.sagepub.com/content/5/1/2.abstract

[45] S. L. Phoenix, Modeling the statistical lifetime of glass fiber/polymer matrix composites in tension, Composite Structures 48 (1–3) (2000) 19 – 29. doi:http://dx.doi.org/10.1016/S0263-8223(99)00069-0.
URL http://www.sciencedirect.com/science/article/pii/S0263822399000690

[46] E. J. Barbero, T. M. Damiani, Phenomenological prediction of tensile strength of e-glass composites from available aging and stress corrosion data, Journal of Reinforced Plastics and Composites 22 (4) (2003) 373–394. arXiv:http://jrp.sagepub.com/content/22/4/373.full.pdf+html, doi:10.1177/0731684403022004269.
URL http://jrp.sagepub.com/content/22/4/373.abstract

[47] N. W. Taylor, Mechanism of fracture of glass and similar brittle solids, Journal of Applied Physics 18 (11) (1947) 943–955. doi:10.1063/1.1697579.

[48] D. A. STUART, O. L. ANDERSON, Dependence of ultimate strength of glass under constant load on temperature, ambient atmosphere, and time, Journal of the American Ceramic Society 36 (12) (1953) 416–424. doi:10.1111/j.1151-2916.1953.tb12831.x.
URL http://dx.doi.org/10.1111/j.1151-2916.1953.tb12831.x

[49] R. J. Charles, Static fatigue of glass. i, Journal of Applied Physics 29 (11) (1958) 1549–1553. doi:http://dx.doi.org/10.1063/1.1722991.
URL http://scitation.aip.org/content/aip/journal/jap/29/11/10.1063/1.1722991

[50] R. J. Charles, Static fatigue of glass. ii, Journal of Applied Physics 29 (11) (1958) 1554–1560. doi:http://dx.doi.org/10.1063/1.1722992.
URL http://scitation.aip.org/content/aip/journal/jap/29/11/10.1063/1.1722992

[51] A. Khennane, R. Melchers, Durability of glass polymer composites subject to stress corrosion, Journal of Composites for Construction 7 (2) (2003) 109–117. arXiv:http://dx.doi.org/10.1061/(ASCE)1090-0268(2003)7:2(109), doi:10.1061/(ASCE)1090-0268(2003)7:2(109).
URL http://dx.doi.org/10.1061/(ASCE)1090-0268(2003)7:2(109)

[52] W. Ren, Investigation on stress-rupture behavior of a chopped-glass-fiber composite for automotive durability design criteria, Tech. Rep. ORNL/TM-2001/106, Metals and Ceramics Division, Oak Ridge National Laboratory (2001).
URL http://web.ornl.gov/~webworks/cppr/y2001/rpt/110965.pdf

[53] M. Phillips, Prediction of long-term stress-rupture life for glass fibre-reinforced polyester composites in air and in aqueous environments, Composites 14 (3) (1983) 270 – 275. doi:http://dx.doi.org/10.1016/0010-4361(83)90015-0.
URL http://www.sciencedirect.com/science/article/pii/0010436183900150

[54] Z. Grasley, D. Lange, Constitutive modeling of the aging viscoelastic properties of portland cement paste, Mechanics of Time-Dependent Materials 11 (3-4) (2007) 175–198. doi:10.1007/s11043-007-9043-4.
URL http://dx.doi.org/10.1007/s11043-007-9043-4

[55] R. Kohlrausch, Theorie des elektrischen rückstandes in der leidner flasche, in: Annalen der Physik, no. 91 in Annalen der Physik, Wiley-VCH, 1854, pp. 56–82,179–213.

[56] G. Williams, D. C. Watts, Non-symmetrical dielectric relaxation behaviour arising from a simple empirical decay function, Trans. Faraday Soc. 66 (1970) 80–85. doi:10.1039/TF9706600080.
URL http://dx.doi.org/10.1039/TF9706600080

[57] L. W. Morland, E. H. Lee, Stress analysis for linear viscoelastic materials with temperature variation, Transactions of The Society of Rheology (1957-1977) 4 (1).

[58] K. Levenberg, A method for the solution of certain non-linear problems in least squares, Quarterly Journal of Applied Mathmatics II (2) (1944) 164–168.

[59] D. Marquardt, An algorithm for least-squares estimation of nonlinear parameters, Journal of the Society for Industrial and Applied Mathematics 11 (2) (1963) 431–441. arXiv:http://dx.doi.org/10.1137/0111030, doi:10.1137/0111030.
URL http://dx.doi.org/10.1137/0111030

[60] T. Williams, C. Kelley, many others, Gnuplot 4.6: an interactive plotting program, http://gnuplot.sourceforge.net/ (November 2014).
URL http://www.gnuplot.info/

[61] R. Schapery, Approximate methods of transform inversion for viscoelastic stress analysis, in: fourth U.S. National Congress of Applied Mechanics, 1962, pp. 1075–1085.

[62] T. L. Cost, E. B. Becker, A multidata method of approximate Laplace transform inversion, International Journal for Numerical Methods in Engineering 2 (2) (1970) 207–219. doi:10.1002/nme.1620020206.
URL http://dx.doi.org/10.1002/nme.1620020206

[63] M. Lévesque, M. Gilchrist, N. Bouleau, K. Derrien, D. Baptiste, Numerical inversion of the Laplace–Carson transform applied to homogenization of randomly reinforced linear viscoelastic media, Computational Mechanics 40 (4) (2007) 771–789. doi:10.1007/s00466-006-0138-6.
URL http://dx.doi.org/10.1007/s00466-006-0138-6

[64] Z. Hashin, Complex moduli of viscoelastic composites—i. general theory and application to particulate composites, International Journal of Solids and Structures 6 (5) (1970) 539 – 552. doi:http://dx.doi.org/10.1016/0020-7683(70)90029-6.
URL http://www.sciencedirect.com/science/article/pii/0020768370900296

[65] Z. Hashin, S. Shtrikman, A variational approach to the theory of the elastic behaviour of multiphase materials, Journal of the Mechanics and Physics of Solids 11 (2) (1963) 127 – 140. doi:10.1016/0022-5096(63)90060-7.
URL http://www.sciencedirect.com/science/article/pii/0022509663900607

[66] Y. Benveniste, A new approach to the application of Mori-Tanaka's theory in composite materials, Mechanics of Materials 6 (2) (1987) 147 – 157. doi:http://dx.doi.org/10.1016/0167-6636(87)90005-6.
URL http://www.sciencedirect.com/science/article/pii/0167663687900056

[67] J. D. Eshelby, The determination of the elastic field of an ellipsoidal inclusion, and related problems, Proceedings of the Royal Society of London. Series A. Mathematical and Physical Sciences 241 (1226) (1957) 376–396. arXiv:http://rspa.royalsocietypublishing.

org/content/241/1226/376.full.pdf+html, doi:10.1098/rspa.1957.0133.
URL http://rspa.royalsocietypublishing.org/content/241/1226/376.abstract

[68] G. Weng, The theoretical connection between Mori-Tanaka's theory and the hashin-shtrikman-walpole bounds, International Journal of Engineering Science 28 (11) (1990) 1111 – 1120. doi:http://dx.doi.org/10.1016/0020-7225(90)90111-U.
URL http://www.sciencedirect.com/science/article/pii/002072259090111U

[69] Y. Zhao, G. Tandon, G. Weng, Elastic moduli for a class of porous materials, Acta Mechanica 76 (1-2) (1989) 105–131. doi:10.1007/BF01175799.
URL http://dx.doi.org/10.1007/BF01175799

[70] W. L. Bond, The mathematics of the physical properties of crystals, Bell System Technical Journal 22 (1) (1943) 1–72. doi:10.1002/j.1538-7305.1943.tb01304.x.
URL http://dx.doi.org/10.1002/j.1538-7305.1943.tb01304.x

[71] B. Auld, B. Auld, Acoustic fields and waves in solids, no. vol. 1 in Acoustic Fields and Waves in Solids, Wiley, 1973.
URL http://books.google.fr/books?id=9_wzAQAAIAAJ

[72] T. Mura, Isotropic inclusions, in: Micromechanics of defects in solids, Vol. 3 of Mechanics of Elastic and Inelastic Solids, Springer Netherlands, 1987, pp. 74–128. doi:10.1007/978-94-009-3489-4_2.
URL http://dx.doi.org/10.1007/978-94-009-3489-4_2

[73] S. Torquato, Random Heterogeneous Materials: Microstructure and Macroscopic Properties, Interdisciplinary Applied Mathematics, Springer, 2002.
URL http://books.google.fr/books?id=PhG_X4-8DPAC

[74] E. Anderson, Z. Bai, J. Dongarra, A. Greenbaum, A. McKenney, J. Du Croz, S. Hammerling, J. Demmel, C. Bischof, D. Sorensen, Lapack: A portable linear algebra library for high-performance computers, in: Proceedings of the 1990 ACM/IEEE Conference on Supercomputing, Supercomputing '90, IEEE Computer Society Press, Los Alamitos, CA, USA, 1990, pp. 2–11.
URL http://dl.acm.org/citation.cfm?id=110382.110385

[75] Z. Bažant, Numerical determination of long-range stress history from strain history in concrete, Matériaux et Construction 5 (3) (1972) 135–141. doi:10.1007/BF02539255.
URL http://dx.doi.org/10.1007/BF02539255

[76] C. Huet, Adaptation d'un algorithme de bazant au calcul des multilames visco-élastiques vieillissants, Matériaux et Construction 13 (2) (1980) 91–98. doi:10.1007/BF02473805.
URL http://dx.doi.org/10.1007/BF02473805

[77] H. Moulinec, P. Suquet, A numerical method for computing the overall response of nonlinear composites with complex microstructure, Computer Methods in Applied Mechanics and Engineering 157 (1–2) (1998) 69 – 94. doi:http://dx.doi.org/10.1016/S0045-7825(97)00218-1.
URL http://www.sciencedirect.com/science/article/pii/S0045782597002181

[78] P. Suquet, H. Moulinec, O. Castelnau, M. Montagnat, N. Lahellec, F. Grennerat, P. Duval, R. Brenner, Multi-scale modeling of the mechanical behavior of polycrystalline ice under transient creep, Procedia {IUTAM} 3 (0) (2012) 76 – 90, iUTAM Symposium on Linking Scales in Computations: From Microstructure to Macro-scale Properties. doi:http://dx.doi.org/10.1016/j.piutam.2012.03.006.
URL http://www.sciencedirect.com/science/article/pii/S2210983812000077

[79] J. Escoda, Modélisation morphologique et micromécanique 3d de matériaux cimentaires, Ph.D. thesis, Mines Paristech (2012).

[80] J. Sliseris, H. Andrä, M. Kabel, B. Dix, B. Plinke, O. Wirjadi, G. Frolovs, Numerical prediction of the stiffness and strength of medium density fiberboards, Mechanics of Materials 79 (0) (2014) 73 – 84. doi:http://dx.doi.org/10.1016/j.mechmat.2014.08.005.
URL http://www.sciencedirect.com/science/article/pii/S0167663614001616

[81] J. Feder, Random sequential adsorption, Journal of Theoretical Biology 87 (2) (1980) 237 – 254. doi:http://dx.doi.org/10.1016/0022-5193(80)90358-6.
URL http://www.sciencedirect.com/science/article/pii/0022519380903586

[82] D. Bentz, E. J. Garboczi, K. A. Snyder, A hard core/soft shell microstructural model for studying percolation and transport in three-dimensional composite media, Tech. rep., National Institute of Standards and Technology (1999).

[83] Y. Pan, L. Iorga, A. A. Pelegri, Analysis of 3d random chopped fiber reinforced composites using FEM and random sequential adsorption, Computational Materials Science 43 (3) (2008) 450 – 461. doi:http://dx.doi.org/10.1016/j.commatsci.2007.12.016.
URL http://www.sciencedirect.com/science/article/pii/S0927025607003515

[84] E. Gilbert, D. Johnson, S. Keerthi, A fast procedure for computing the distance between complex objects in three space, in: Robotics and Automation. Proceedings. 1987 IEEE International Conference on, Vol. 4, 1987, pp. 1883–1889. doi:10.1109/ROBOT.1987.1087825.

[85] F. Lavergne, K. Sab, J. Sanahuja, M. Bornert, C. Toulemonde, Investigation of the effect of aggregates' morphology on concrete creep properties by numerical simulations, Cement and Concrete Research 71 (0) (2015) 14 – 28. doi:http://dx.doi.org/10.1016/j.cemconres.2015.01.003.
URL http://www.sciencedirect.com/science/article/pii/S0008884615000101

[86] O. Zienkiewicz, M. Watson, I. King, A numerical method of visco-elastic stress analysis, International Journal of Mechanical Sciences 10 (10) (1968) 807 – 827. doi:10.1016/0020-7403(68)90022-2.
URL http://www.sciencedirect.com/science/article/pii/0020740368900222

[87] R. L. Taylor, K. S. Pister, G. L. Goudreau, Thermomechanical analysis of viscoelastic solids, International journal for numerical methods in engineering 2 (1970) 45–59.

[88] Z. P. Bažant, S. T. Wu, Creep and shrinkage law for concrete at variable humidity, Journal of the Engineering Mechanics Division 100 (6) (1974) 1183–1209.

[89] K. Sab, On the homogenization and the simulation of random materials, European Journal of Mechanics A-Solids 11 (5) (1992) 585–607.

[90] T. Kanit, S. Forest, I. Galliet, V. Mounoury, D. Jeulin, Determination of the size of the representative volume element for random composites: statistical and numerical approach, International Journal of Solids and Structures 40 (13–14) (2003) 3647 – 3679. doi:http://dx.doi.org/10.1016/S0020-7683(03)00143-4.
URL http://www.sciencedirect.com/science/article/pii/S0020768303001434

[91] F. Lavergne, R. Brenner, K. Sab, Effects of grain size distribution and stress heterogeneity on yield stress of polycrystals: A numerical approach, Computational Materials Science 77 (0) (2013) 387 – 398. doi:http://dx.doi.org/10.1016/j.commatsci.2013.04.061.
URL http://www.sciencedirect.com/science/article/pii/S0927025613002334

[92] J. M. Hedgepeth, Stress concentrations in filamentary structures, Tech. Rep. NASA-TN-D-882, L-1502, NASA Langley Research Center; Hampton, VA United States (1961).
URL http://ntrs.nasa.gov/search.jsp?R=19980227450

[93] I. J. Beyerlein, C. M. Landis, Shear-lag model for failure simulations of unidirectional fiber composites including matrix stiffness, Mechanics of Materials 31 (5) (1999) 331 – 350. doi:http://dx.doi.org/10.1016/S0167-6636(98)00075-1.
URL http://www.sciencedirect.com/science/article/pii/S0167663698000751

[94] S. Blassiau, A. Thionnet, A. Bunsell, Three-dimensional analysis of load transfer micromechanisms in fibre/matrix composites, Composites Science and Technology 69 (1) (2009) 33 – 39, mechanical Response of Fibre Reinforced Composites. doi:http://dx.doi.org/10.1016/j.compscitech.2007.10.041.
URL http://www.sciencedirect.com/science/article/pii/S0266353807004381

[95] N. Kotelnikova-Weiler, J.-F. Caron, O. Baverel, Kinetic of fibre ruptures in a UD

composite material with a viscoelastic matrix subject to traction [Cinétique de ruptures de fibres dans un matériau composite UD soumis à la traction avec une matrice viscoélastique], Revue des composites et des matériaux avancés 23 (1) (2013) 125–138. doi:10.3166/rcma.23.125-138.
URL https://hal-enpc.archives-ouvertes.fr/hal-00946107

[96] W. Yang, Y. Pan, A. A. Pelegri, Multiscale modeling of matrix cracking coupled with interfacial debonding in random glass fiber composites based on volume elements, Journal of Composite Materials 47 (27) (2013) 3389–3399. arXiv:http://jcm.sagepub.com/content/47/27/3389.full.pdf+html, doi:10.1177/0021998312465977.
URL http://jcm.sagepub.com/content/47/27/3389.abstract

[97] T. Baxevanis, N. Charalambakis, A micromechanically based model for damage-enhanced creep-rupture in continuous fiber-reinforced ceramic matrix composites, Mechanics of Materials 42 (5) (2010) 570 – 580. doi:http://dx.doi.org/10.1016/j.mechmat.2010.02.004.
URL http://www.sciencedirect.com/science/article/pii/S0167663610000268

[98] H. Stehfest, Algorithm 368: Numerical inversion of Laplace transforms [d5], Commun. ACM 13 (1) (1970) 47–49. doi:10.1145/361953.361969.
URL http://doi.acm.org/10.1145/361953.361969

[99] W. Whitt, A unified framework for numerically inverting Laplace transforms, INFORMS Journal on Computing 18 (2006) 408–421.

[100] D. J. Eyre, G. W. Milton, A fast numerical scheme for computing the response of composites using grid refinement, The European Physical Journal Applied Physics 6 (1999) 41–47. doi:10.1051/epjap:1999150.
URL http://www.epjap.org/article_S1286004299001500

[101] V. Monchiet, G. Bonnet, A polarization-based FFT iterative scheme for computing the effective properties of elastic composites with arbitrary contrast, International Journal for Numerical Methods in Engineering 89 (11) (2012) 1419–1436. doi:10.1002/nme.3295.
URL http://dx.doi.org/10.1002/nme.3295

[102] H. Moulinec, F. Silva, Comparison of three accelerated FFT-based schemes for computing the mechanical response of composite materials, International Journal for Numerical Methods in Engineering 97 (13) (2014) 960–985. doi:10.1002/nme.4614.
URL http://dx.doi.org/10.1002/nme.4614

[103] S. Zhurkov, Kinetic concept of the strength of solids, International Journal of Fracture 26 (4) (1984) 295–307. doi:10.1007/BF00962961.
URL http://dx.doi.org/10.1007/BF00962961

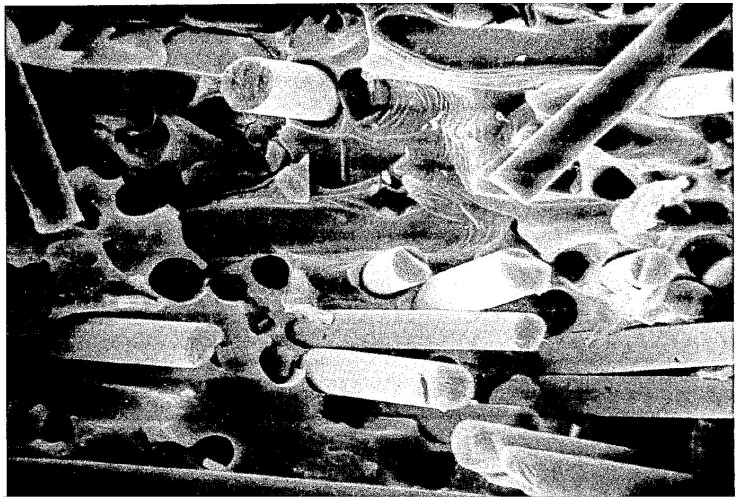

(a) photomicrograph of a cross section of a fiber-reinforced plastic, the cross section being of a fractured tensile dumb-bell [3]. The distribution of the orientations of fibers does not seem isotropic and this particular sample exhibits fiber-matrix debonding. The failure mode highly depends on the coupling agent[3].

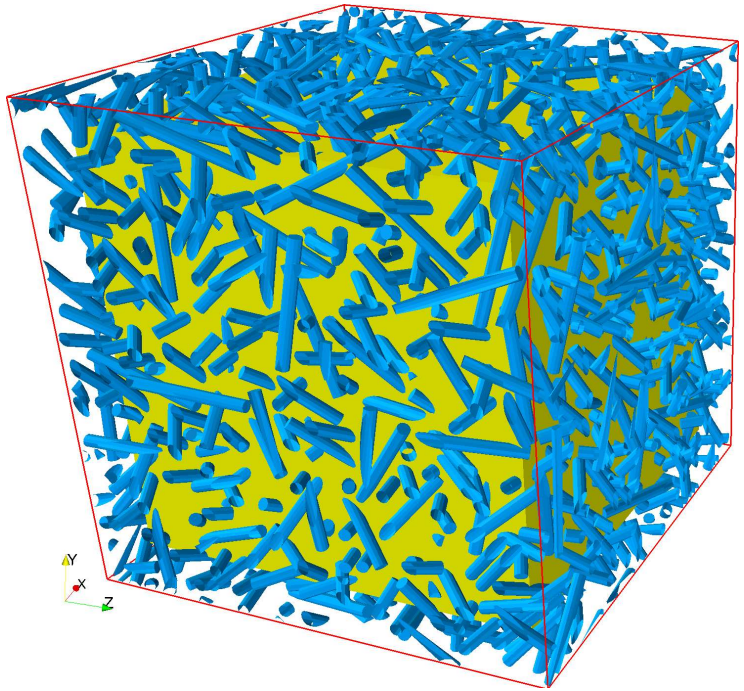

(b) a 400μm-wide sample of a fiber-reinforced plastic by the RSA algorithm is shown. The volume fraction of fibers in the cubic cell is 15%. Fibers are 10μm in diameter and 100μm in length.

Figure 1: Real and numerical microstructures.

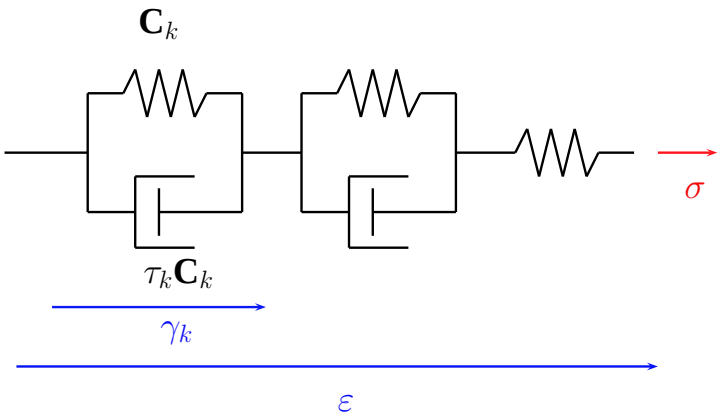

Figure 2: A rheological model made of a series of Kelvin chains

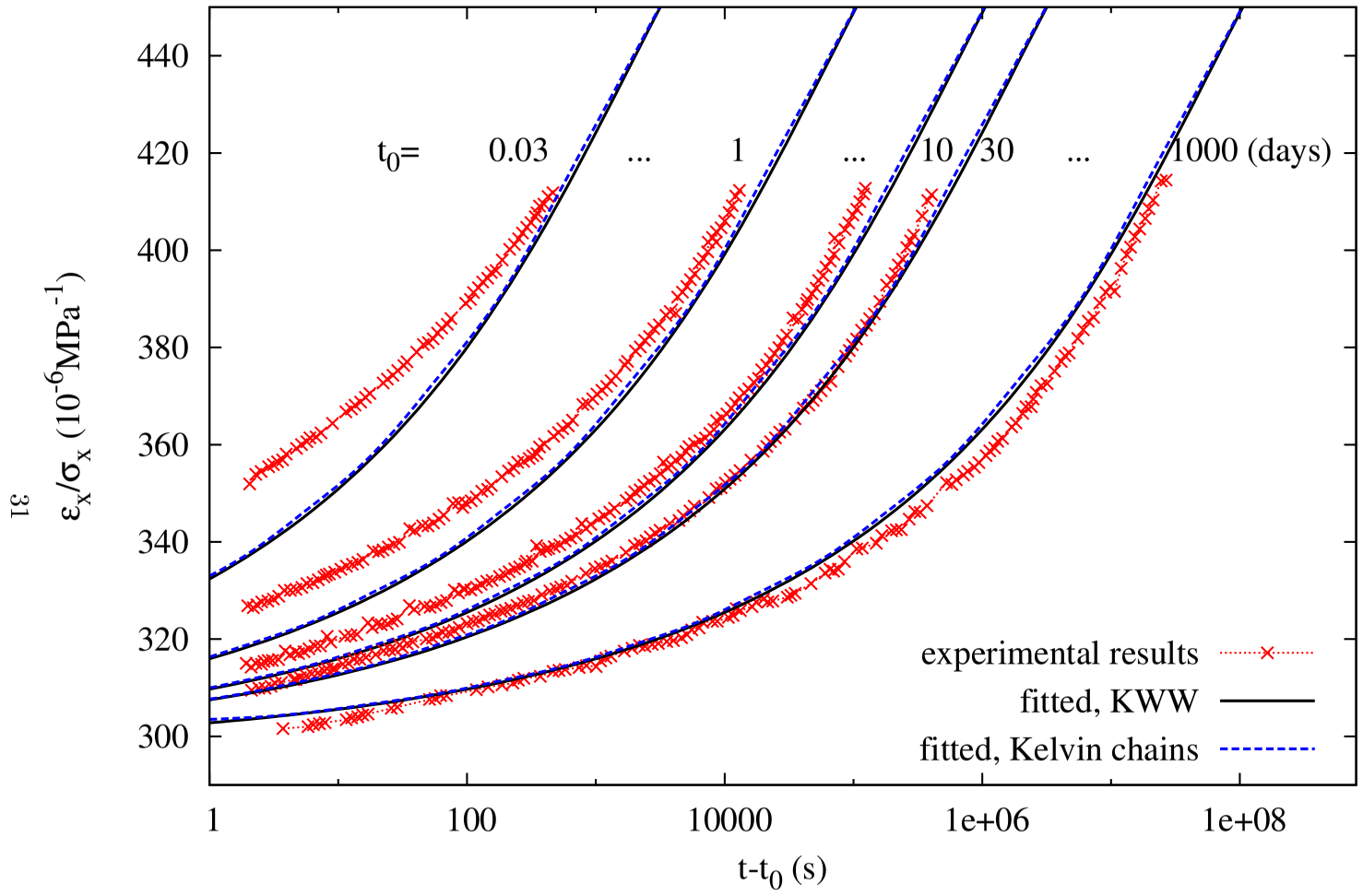

Figure 3: The experimental results of Struik [15] on hard polyvinyl chloride (PVC) at T=20°C are digitalized. First parameters of aging μ and of the KWW function are fitted according to some of these curves ($t_0 = 10, 30, 100, 300$ and 1000 days). Then a series of Kelvin chains is adjusted to the KWW function to enable 3D numerical computations (blue).

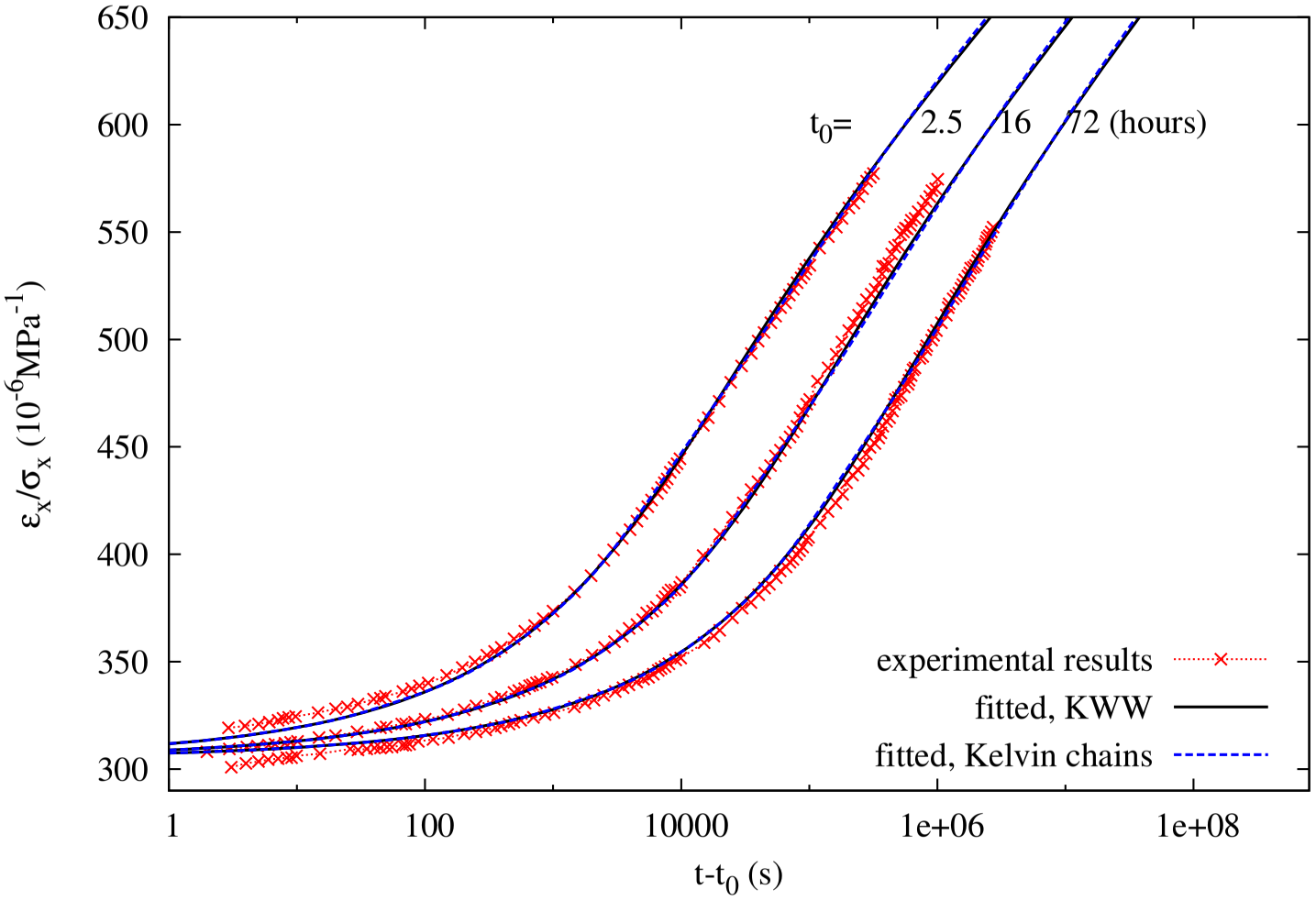

Figure 4: The experimental results of Read et. al. [18] on hard polyvinyl chloride (PVC) at T=23°C are digitalized. First parameters of aging μ and of the KWW function are fitted according to these curves. Then a series of Kelvin chains is adjusted to the KWW function to enable 3D numerical computations (blue).

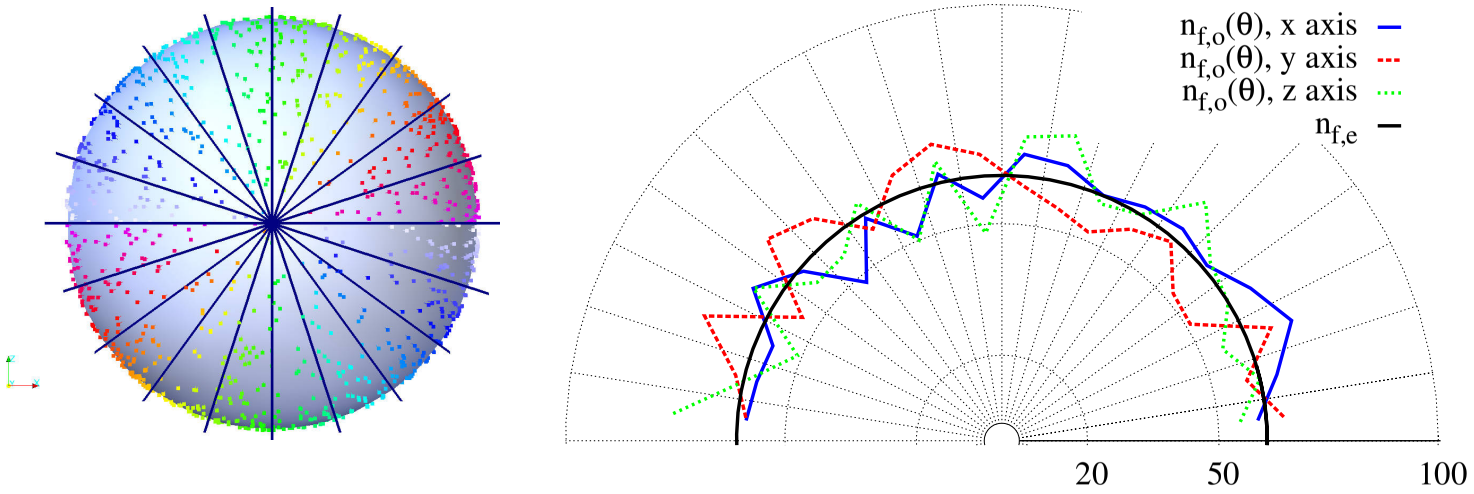

Figure 5: Left : fiber orientations are binned into 20 sectors of equal angle along y axis. Right : the estimated number of fiber in each sector $n_{f,e} = 61,1$ is compared to the observed ones $n_{f,o}(\theta)$, $\theta \in 1..20$. An isotropic distribution of orientation can produce such a set of observations.

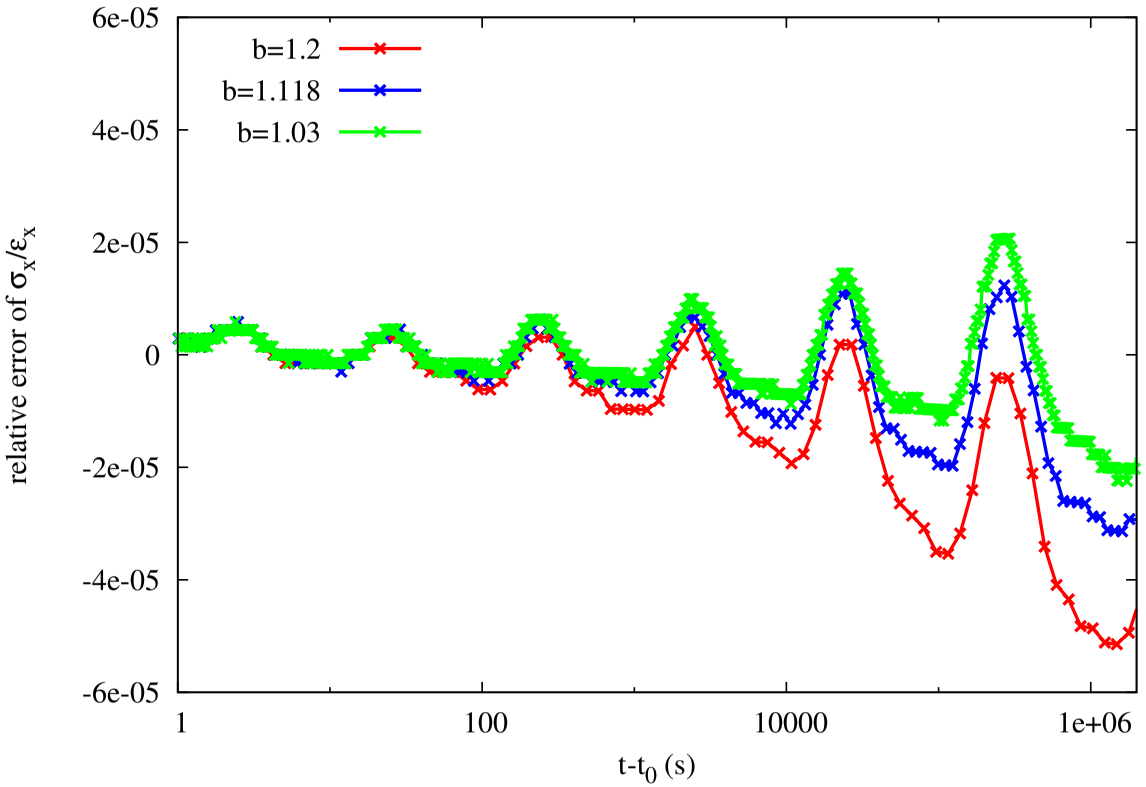

Figure 6: Relative error due to time stepping. Numerical relaxation tests are performed on the matrix for different rate of growth of the time step $b = (t_{i+1} - t_i)/(t_i - t_{i-1})$. The relative error decreases as the time steps decrease. Rises correspond to characteristic times of Kelvin chains. The relative error seems discrete due to numbers being stored in files as single-precision floats.

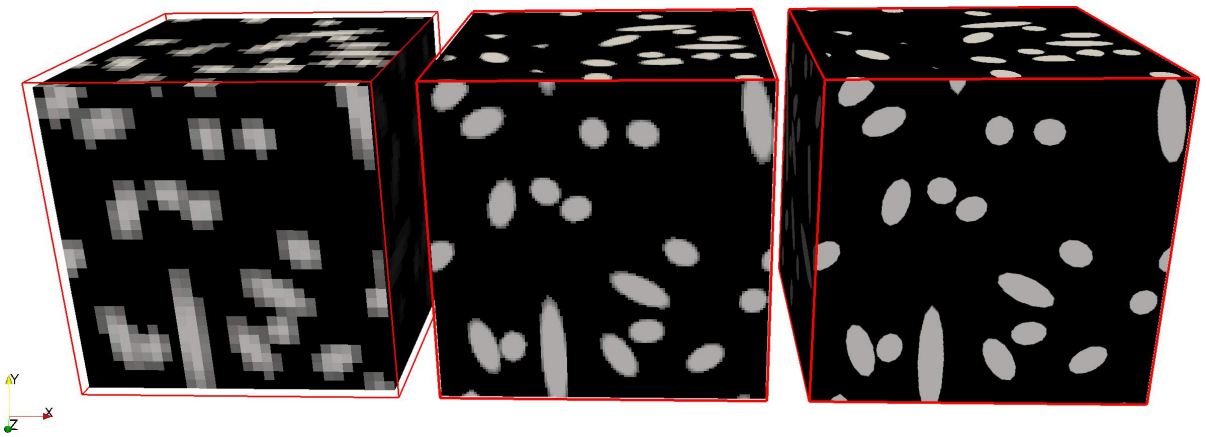

Figure 7: The same microstructure of length 133μm is discretized on grids of size $N = 32$, $N = 128$ and $N = 648$. Hence the corresponding total numbers of voxels are respectively 32^3, 128^3 and 648^3. Cross sections of cylindrical fibers are ellipses, except at edges.

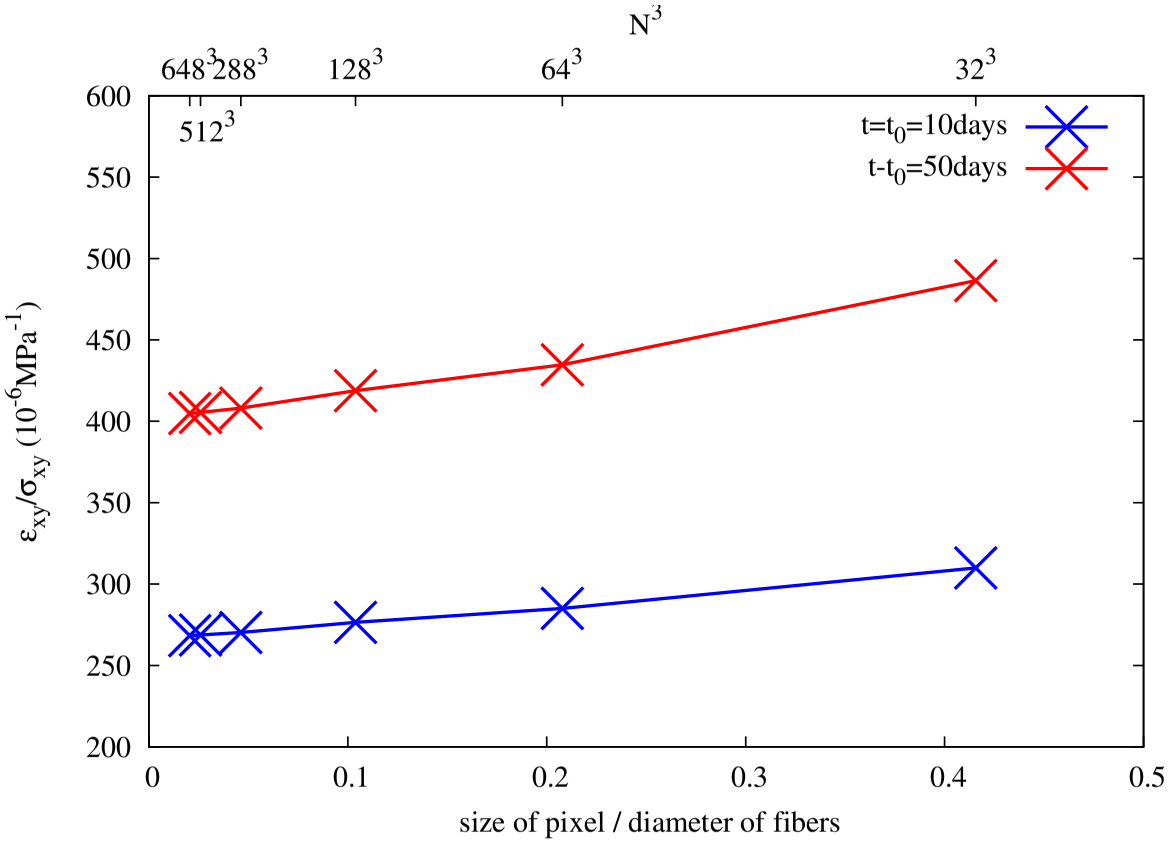

Figure 8: The estimated instantaneous strain ε_{xy} and the estimated strain 50 days after loading are plotted as a functions of the grid size N. A grid size corresponds to a ratio between the size of the pixel and the diameter of the fibers.

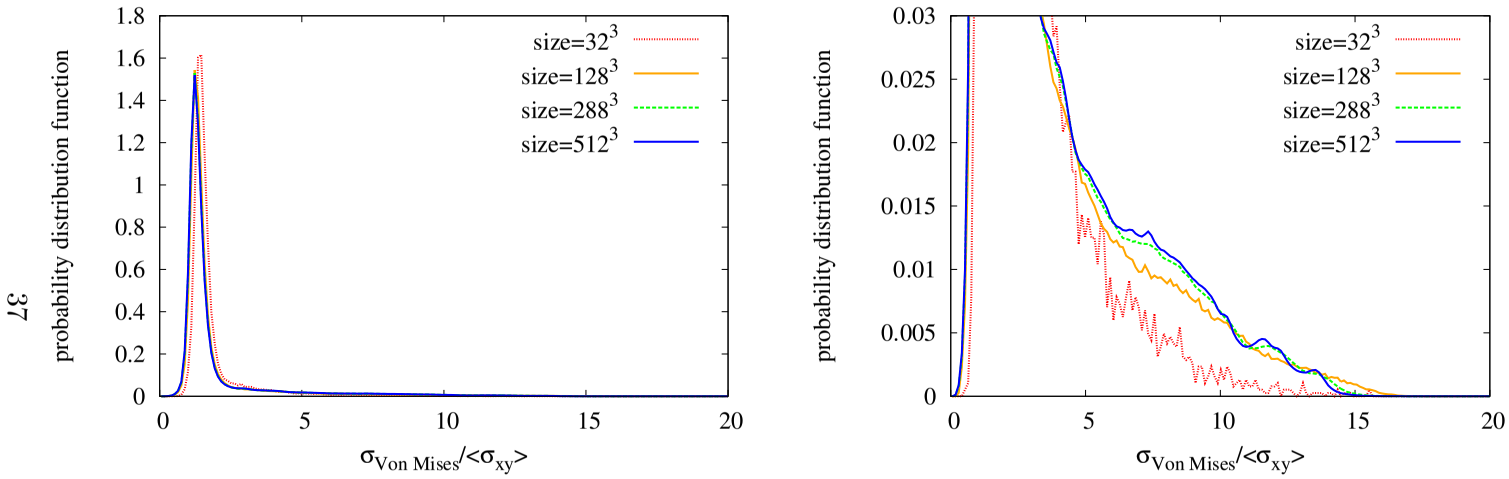

Figure 9: The elastic response to a shear stress at $t_0 = 10$ days is computed and probability distribution functions of the Von Mises stress are displayed for different grid size N. On the right: the prediction of large stress concentrations becomes more and more accurate as the grid size N increases. The focus on large stress concentrations helps defining an accurate failure criteria.

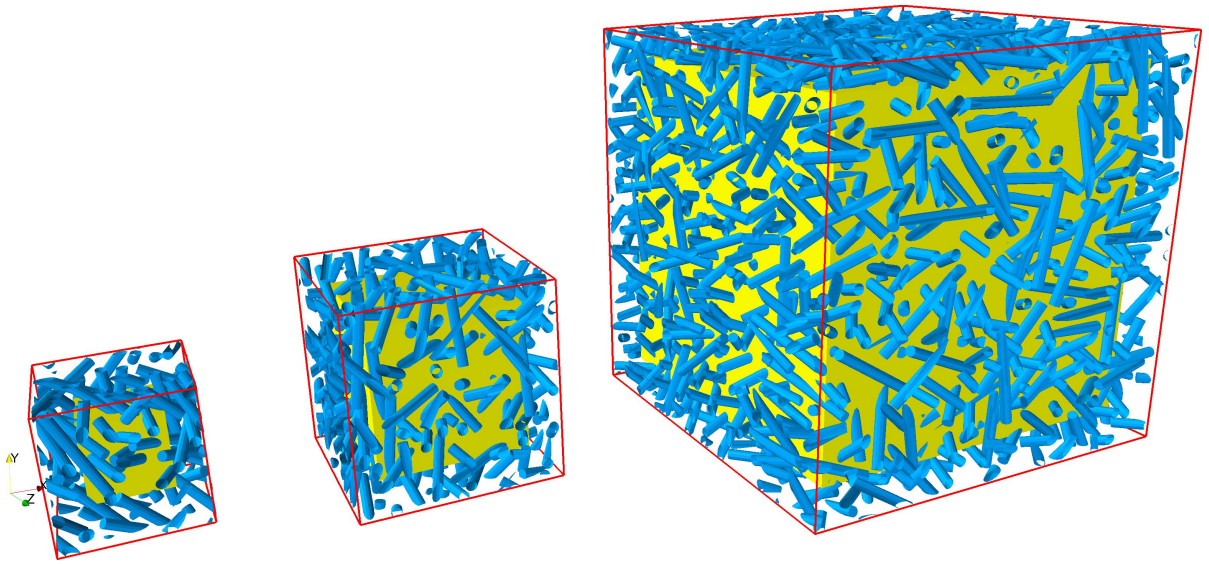

(a) Unit cells of sizes $l = 133\mu$m, 200μm and 400μm are respectively discretized on grids of sizes $N = 128$, $N = 192$ and $N = 384$.

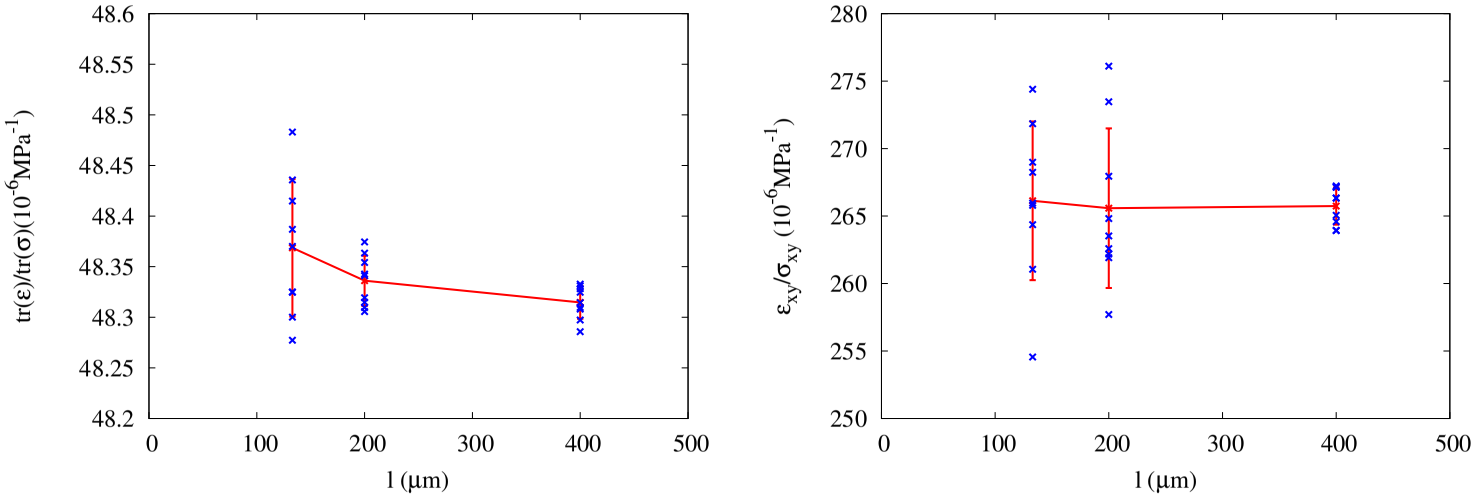

(b) On the left, the overall responses to an hydrostatic stress is displayed as a function of the size of the unit cell. On the right, a shear stress is considered. The red lines and error bars correspond to averages and standard deviation respectively. As the size of the unit cell increases, the estimate of the overall response becomes less variable.

Figure 10: The elastic response of unit cells of different sizes l at $t_0 = 10$ days is computed.

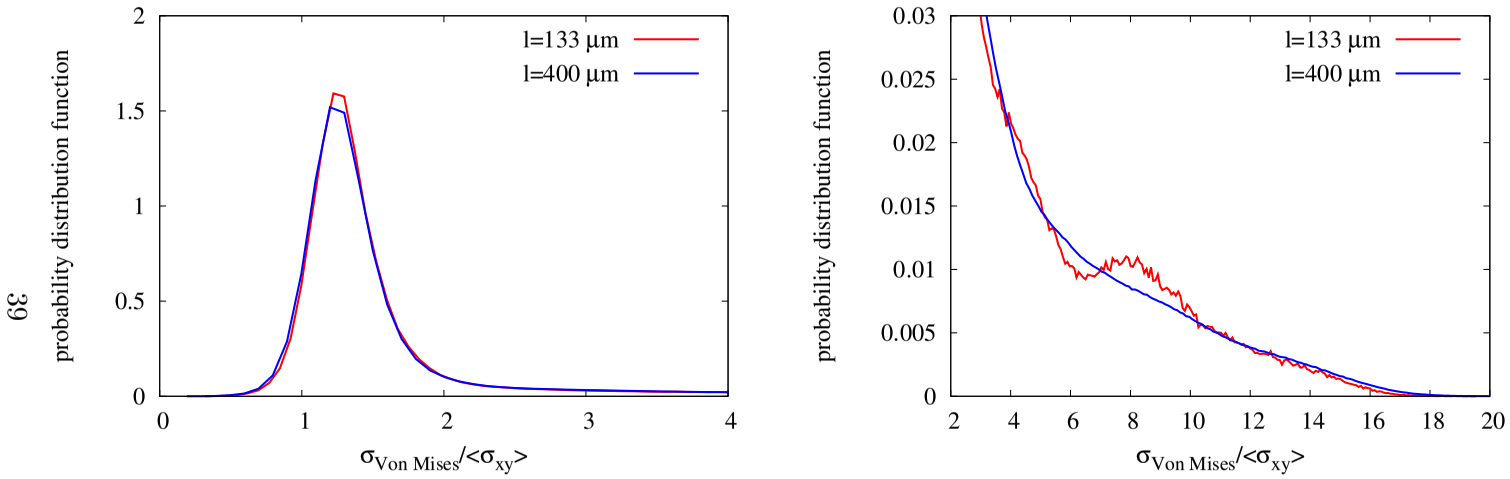

Figure 11: Left: the estimate of the probability distribution function of the Von Mises stress depends slightly on the size of the unit cell l (left). Right: a focus on large stress concentrations is displayed. The hump at $l = 133\mu$m is due to a lack of representativity of the unit cell. As l increases, the probability distribution becomes smoother.

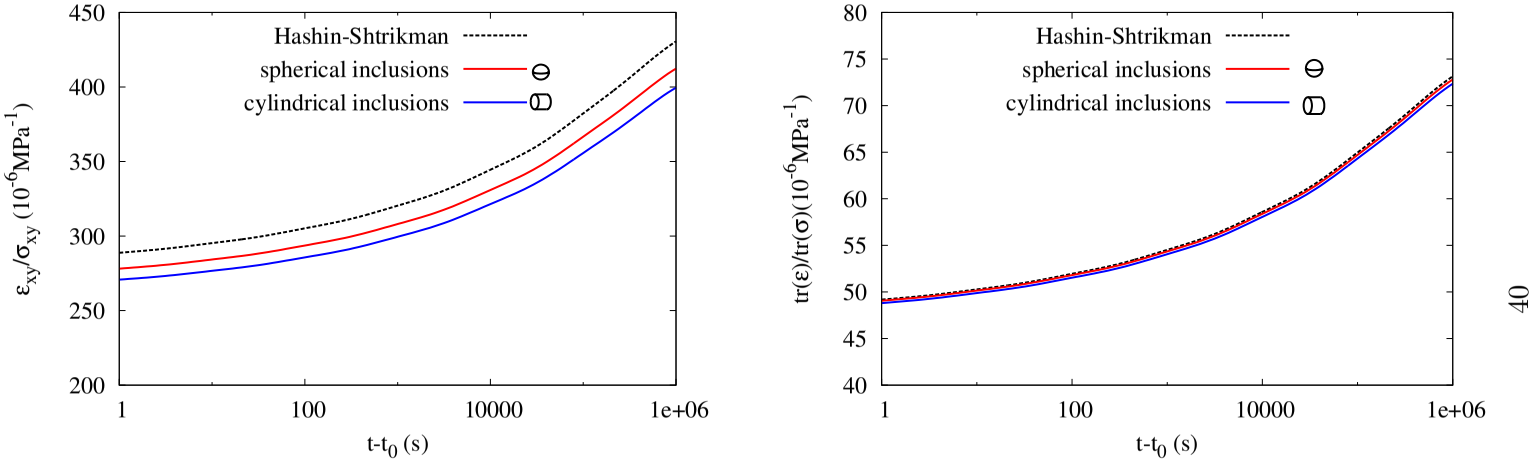

Figure 12: Overall responses estimated by the Hashin-Shtrikman scheme (dashed lines) and 3D numerical computations (solid lines) for glass-reinforced PVC featuring different shapes of inclusions. A shear creep test $\sigma_{xy} = 1$ (left) and a hydrostatic creep test $tr(\sigma) = 1$ (right) are performed. The volume fraction of fibers is 20%. $N = 384$, $l = 80\mu$m.

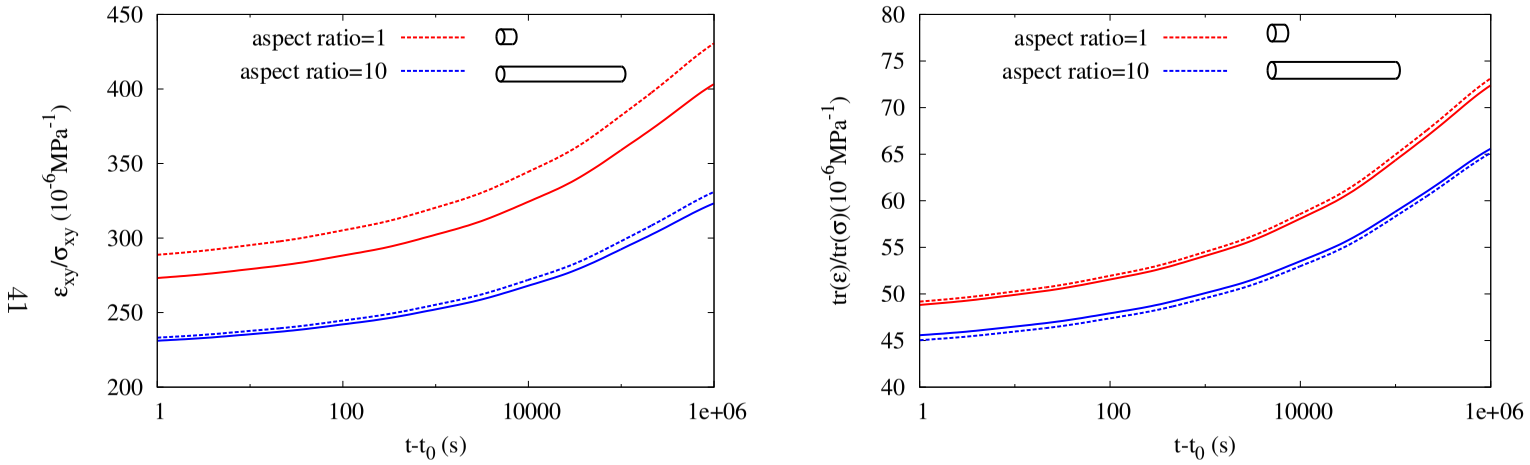

Figure 13: Overall responses estimated by the Mori-Tanaka scheme (dashed lines) and 3D numerical computations (solid lines) for fiber-reinforced polymers featuring different lengths of fibers. A shear creep test $\sigma_{xy} = 1$ (left) and a hydrostatic creep test $tr(\sigma) = 1$ (right) are performed. The Mori-Tanaka scheme manages to capture the influence of the aspect ratio. The volume fraction of fibers is 20%.

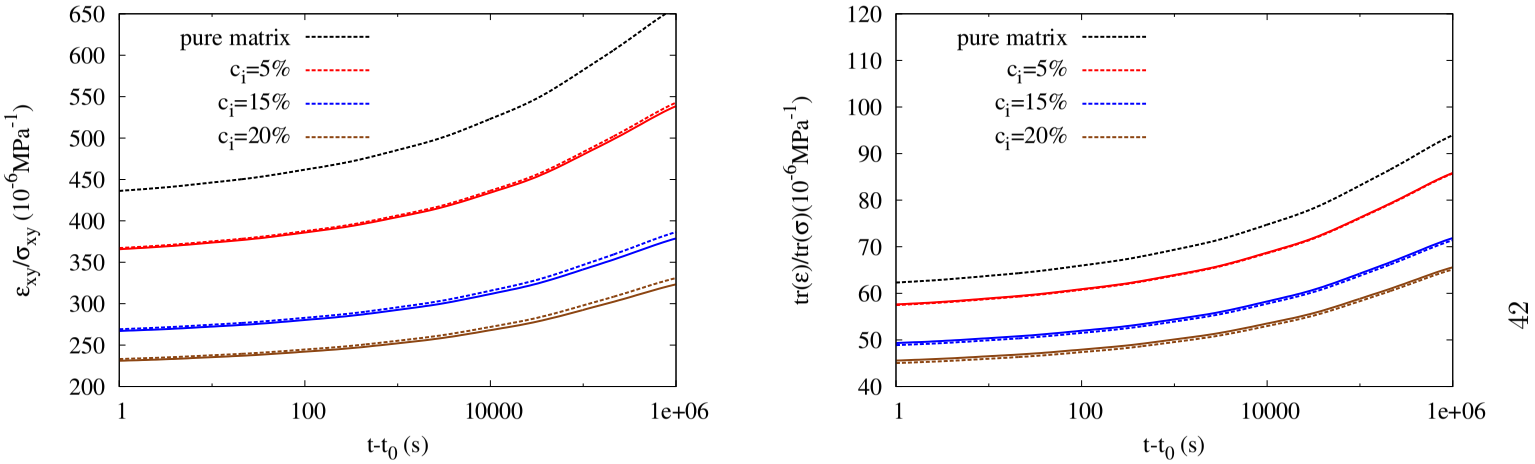

Figure 14: Overall responses estimated by the Mori-Tanaka scheme (dashed lines) and 3D numerical computations (solid lines) for fiber-reinforced polymers featuring different volume fractions of fibers. A shear creep test $\sigma_{xy} = 1$ (left) and a hydrostatic creep test $tr(\sigma) = 1$ (right) are performed. The Mori-Tanaka estimates match the numerical one. The length of fibers is 100μm, corresponding to an aspect ratio of 10.

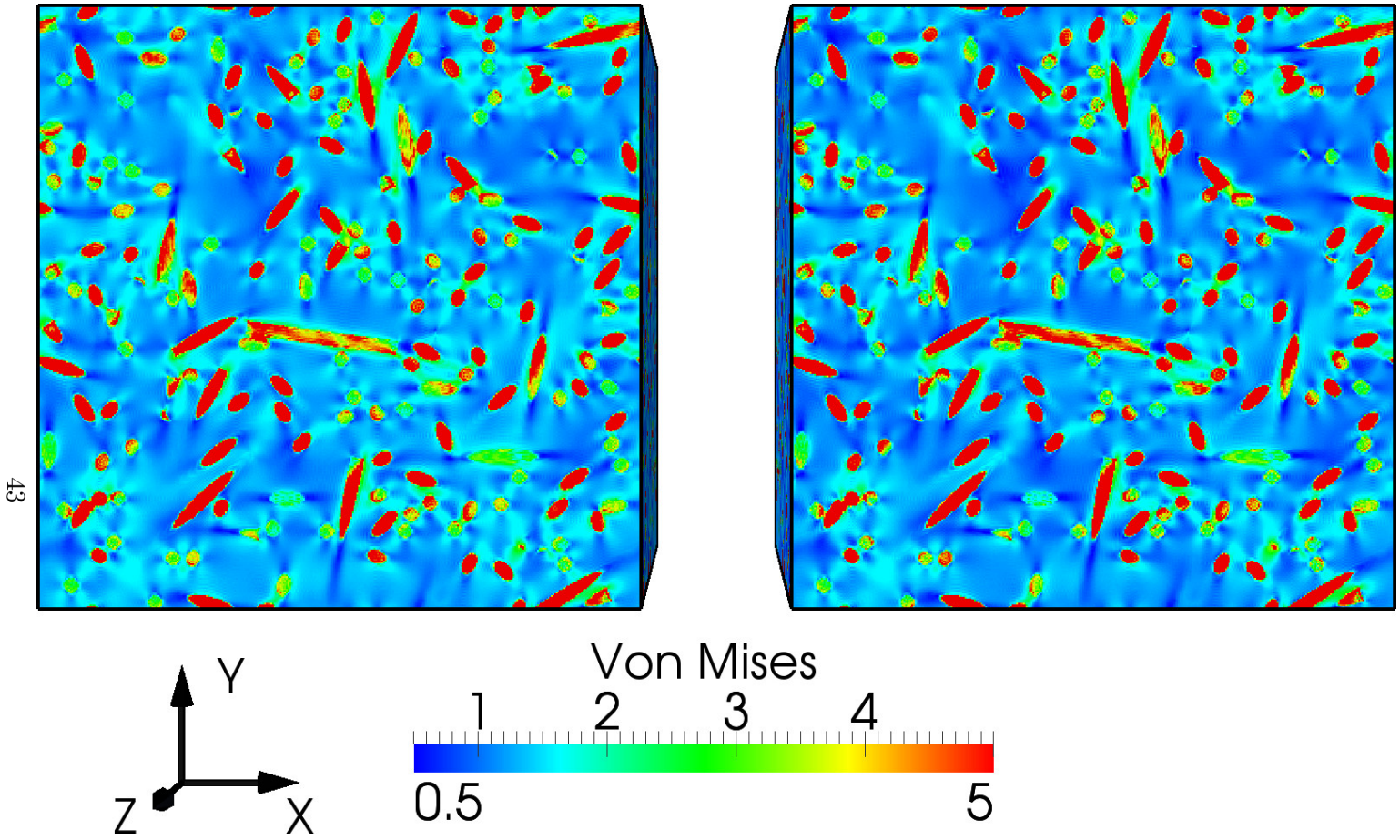

Figure 15: Stress concentrations in a a fiber-reinforced polymer may be estimated by 3D numerical computations. A numerical shear creep test $\sigma_{xy} = 1$ is performed and the Von Mises stress is displayed at $t - t_0 = 0$ (left) and $t - t_0 = 50$ days (right). It is noticeable that the Von Mises stress is highly variable in the matrix. These stress concentrations do not change much over time: the fibers already bear much of the loading at the time of loading. $N = 384$, $l = 200\mu$m

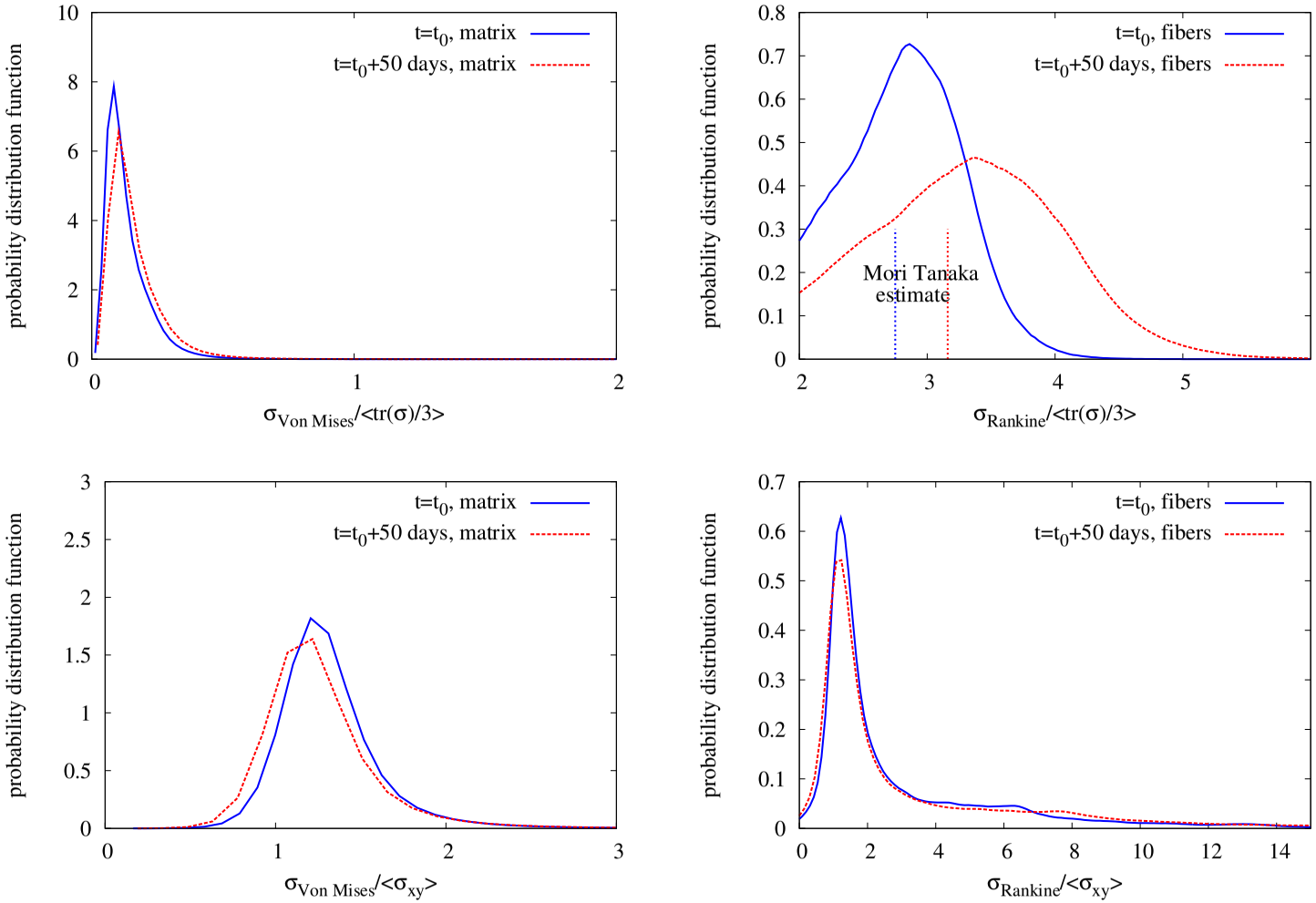

Figure 16: The estimate of the probability distribution function of the Von Mises stress stress in the matrix and Rankine criteria in fibers during an hydrostatic creep test (top) and a shear creep test (bottom). Stress concentrations do not change largely during creep tests: inclusions already bear a large part of the loading at $t = t_0$. Top right: the Rankine criteria increase in fibers during an hydrostatic creep test. The numerical results are compared to the Mori-Tanaka estimates. $N = 384$, $l = 200\mu$m

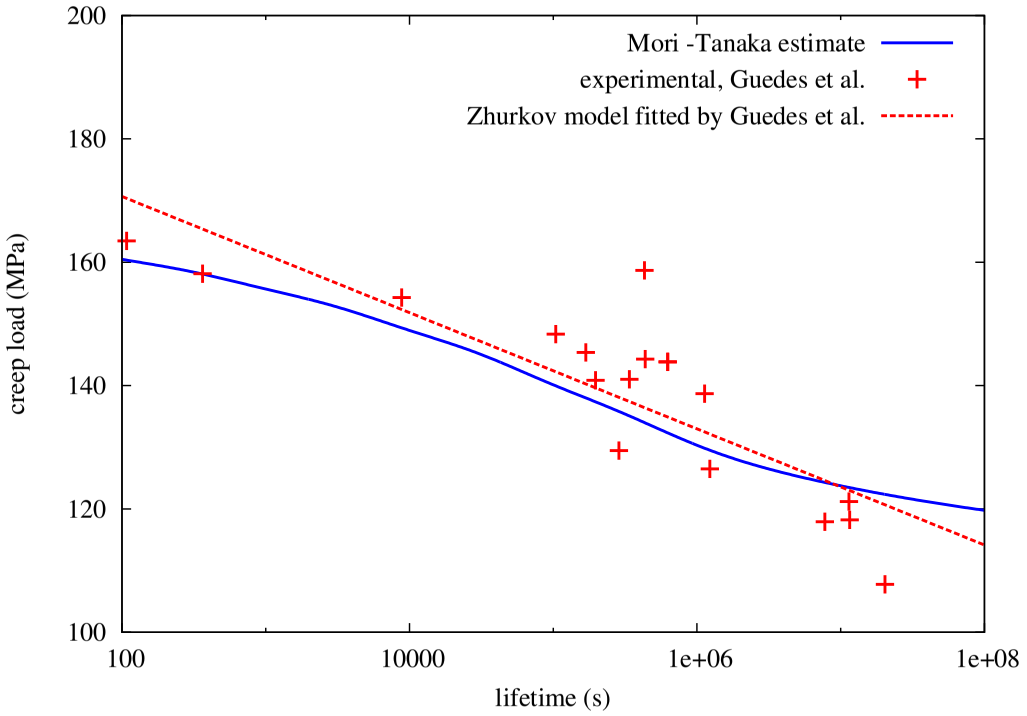

Figure 17: The Mori-Tanaka estimate of the lifetime versus the creep load. The volume fraction of fibers is 15% and their aspect ratio is 300, corresponding to 3mm-long fibers. The material is loaded at 10 days. The strength of fiber is set at $\sigma_c^{MT} = 2.4$GPa so that the estimated instantaneous tensile strength is close to the one measured by Guedes et al.[14]. The Zhurkov model of creep failure [103] is a straight line $t/\tau = e^{U-\gamma\sigma}$ adjusted by Guedes et al. on their experimental data (τ=3600s, U=38.1MPa,$\gamma = 0.24$.

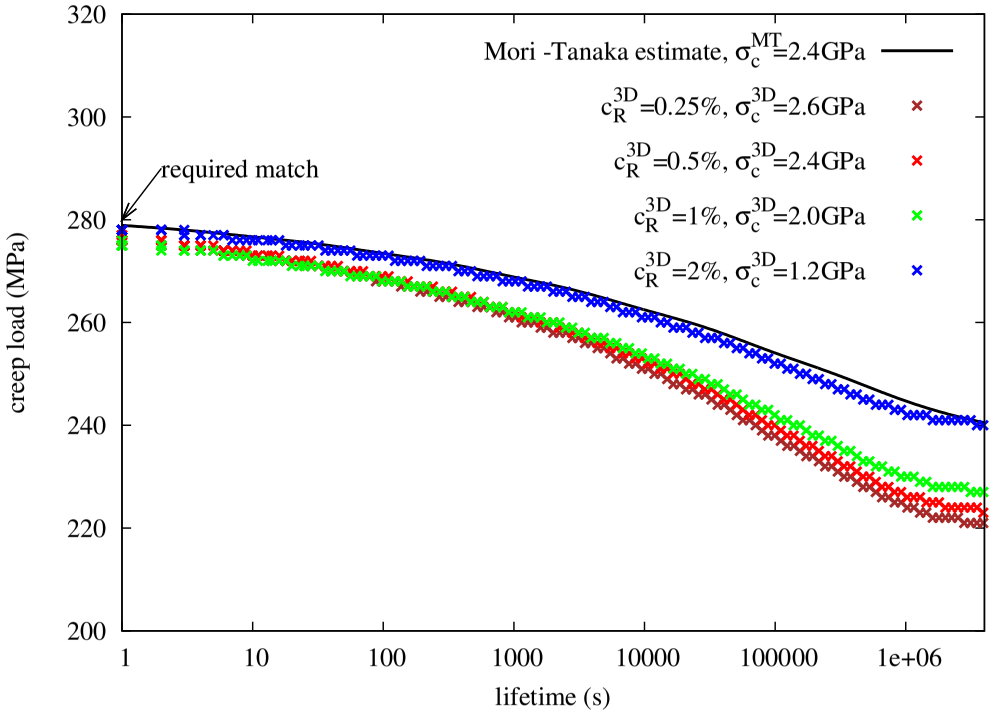

Figure 18: The Mori-Tanaka estimate and numerical estimates of the lifetime versus the creep load. The volume fraction of fibers is 15% and their aspect ratio is 10, corresponding to 100μm-long fibers. The material is loaded at 10 days. The grid size is $N = 384$ and $l = 200\mu$m. The 3D criteria depends on parameters c_R^{3D} and σ_c^{3D}, which can be adjusted to match the Mori-Tanaka estimate.

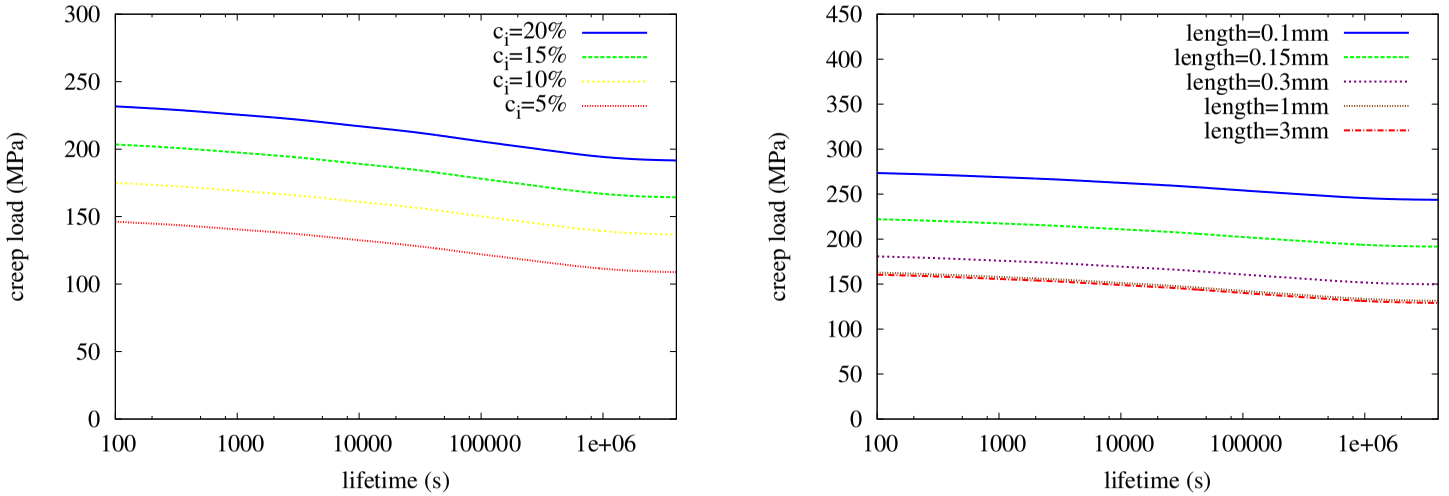

Figure 19: The Mori-Tanaka estimate of the lifetime versus the uniaxial traction creep load. Left: effect of the volume fraction of fibers, the length of fibers being 1mm. Right: Effect of the length of fibers, the volume fraction of fibers being 15%. If fibers are more than 1mm long, the size of the fiber has little effect on tensile strength or creep failure. Fiber lengths lower than 300μm may improve the mechanical performance of the composite, but the polymer may become the limiting factor.

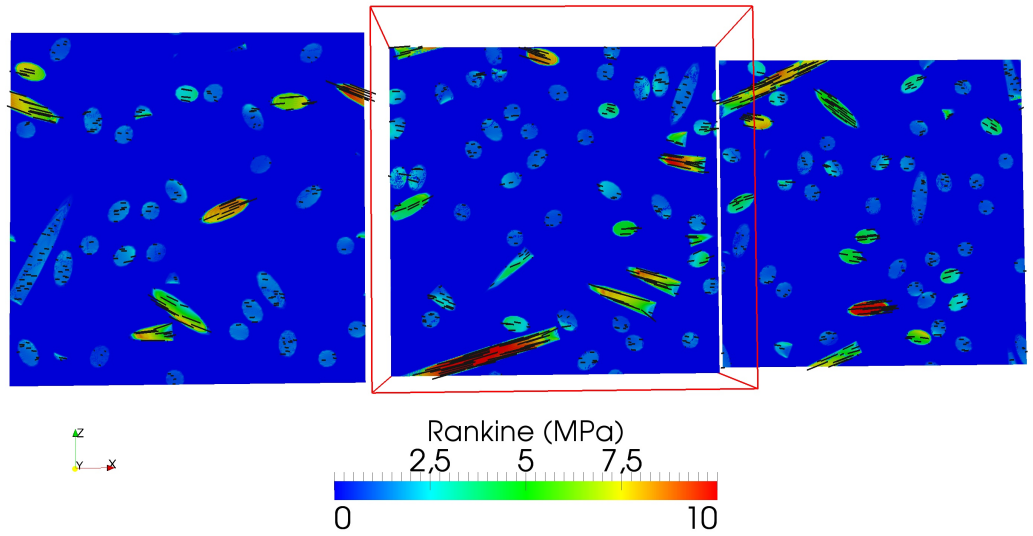

Figure 20: The Rankine criteria in fibers as computed by 3D numerical computation of an uniaxial creep test $\sigma_x = 1$MPa. Three slices are displayed. Fibers parallel to axis x feature larger Rankine criteria. Black lines correspond to the direction of the maximal principal stress in fiber. This direction is parallel to the axis of the fiber.

μ	τ_{ref} (s)
-0.99998	1

(a) Aging parameters

$\mathbf{E}_0$ (GPa)	τ_0(s)	m
3.37	135	0.17

(b) KWW function

$\mathbf{E}_0$ (GPa)	ν
80	0.22

(c) Fibers

i	τ_i (s)	$\mathbf{E}_i$ (GPa)
0	instantaneous	3.3
1	5×10^{-8}	347
2	5×10^{-7}	224
3	5×10^{-6}	152
4	5×10^{-5}	99
5	5×10^{-4}	66
6	5×10^{-3}	40.8
7	5×10^{-2}	27.4
8	5×10^{-1}	11.8

(d) Kelvin chains

Table 1: Values fitted according to the experimental results of Struik [15] on rigid PVC at T=20°C and values for E-glass fibers. All Poisson's ratios of PVC are assumed to be 0.40. The aging coefficient μ is set at -0.99998.

μ	τ_{ref} (s)
-0.958	1

(a) Aging parameters

$\mathbf{E}_0$ (GPa)	τ_0(s)	m
3.28	22.5	0.324

(b) KWW function

$\mathbf{E}_0$ (GPa)	ν
80	0.22

(c) Fibers

i	τ_i (s)	$\mathbf{E}_i$ (GPa)
0	instantaneous	3.27
1	4.8×10^{-6}	906
2	4.8×10^{-5}	387
3	4.8×10^{-4}	198
4	4.8×10^{-3}	83.9
5	4.8×10^{-2}	43.0
6	4.8×10^{-1}	16.5
7	4.8×10^{0}	9.21
8	4.8×10^{1}	1.23

(d) Kelvin chains

Table 2: Values fitted according to the experimental results of Read et. al. [18] on rigid PVC, at T=23°C. All Poisson's ratios of hard PVC are assumed to be 0.40. Both the values of the aging parameter $\mu = -0.958$ and the shape parameter $m = 0.324$ are close to the values identified by Struik or Read et. al. [15, 18]

N	number of degree of freedom	number of nodes (cluster)	number of processes	wall-clock time s
32	2×10^5	1	4	86
64	1.5×10^6	1	4	756
128	1.2×10^7	1	12	4012
288	1.4×10^8	12	144	4225
512	8×10^8	12	128	29440
648	1.6×10^9	16	162	47490

Table 3: Grid sizes and numerical performances on the Ivanhoé cluster of EDF R&D (iDataPlex, Xeon X5670 6C 2.93 GHz, Infiniband). Increasing the memory bandwidth by using twelve nodes instead of one allows a tenfold increase of the number of degrees of freedom while keeping comparable wall-clock times.